†Corresponding email address: sandy.herho@email.ucr.edu

Topological and Information-Theoretic Analysis of Climate-Driven Indonesian Throughflow Dynamics

Sandy H. S. Herho[1*], Katarina E. P. Herho[2], Iwan P. Anwar[3], Rusmawan Suwarman[4]

[1*]Department of Earth and Planetary Sciences, University of California, Riverside, 900 University Ave., Riverside, 92521, CA, USA.
[2]Department of Geological Engineering, Trisakti University, Jalan Kyai Tapa 1, West Jakarta, 11440, Special Capital Region of Jakarta, Indonesia.
[3]Oceanography Research Group, Bandung Institute of Technology (ITB), Jalan Ganesha 10, Bandung, 40132, West Java, Indonesia.
[4]Atmospheric Science Research Group, Bandung Institute of Technology (ITB), Jalan Ganesha 10, Bandung, 40132, West Java, Indonesia.

*Corresponding author(s). E-mail(s): sandy.herho@email.ucr.edu;

Abstract

The Indonesian Throughflow (ITF) represents the sole tropical pathway connecting Pacific and Indian Oceans, yet quantitative understanding of climate mode influences on its variability remains incomplete. We applied information-theoretic and topological frameworks to analyze 34 years (1984-2017) of observational ITF transport data alongside ENSO and IOD indices. Bootstrap analysis revealed pronounced ITF seasonality with 13.28 Sv amplitude peaking in September, contrasting with negligible climate index annual cycles, indicating scale separation in forcing mechanisms. Multi-method extrema detection identified 36-41 extreme events per variable, with 23.1% coincidence between ENSO and IOD high extrema confirming known co-occurrence patterns. Ensemble information-theoretic metrics demonstrated ENSO exerts moderately stronger influence on ITF (mean score 0.524) compared to IOD (0.500), with component-specific optimal lag relationships ranging 4-9 months. Transfer entropy quantified directional information flow with causality ratios of 0.528-0.571. Topological analysis through persistent homology identified stable second homology features (7-11 voids) across climate states, suggesting robust dynamical constraints. Two regime shifts were detected with 100% accuracy and 2.3-month average lead time during near-neutral climate conditions. Extended predictive lead times (22-33 months) indicate gradual phase space reorganization preceding transport anomalies. These findings demonstrate nonlinear analytical frameworks reveal climate-ocean coupling mechanisms obscured by traditional approaches, with implications for improving ITF projections under changing climate.

Keywords: Climate variability, Indonesian Throughflow, Information theory, Persistent homology, Transfer entropy

1 Introduction

The Indonesian Throughflow (ITF) represents the sole tropical oceanic pathway connecting the Pacific and Indian Oceans, serving as a critical chokepoint in the global ocean circulation system [1, 2]. This unique inter-basin exchange transfers approximately 15 Sverdrups in 3-year period (1 Sv $\equiv 10^6$ m^3 s^{-1}) of warm, relatively fresh Pacific waters into the Indian Ocean through a complex network of straits and passages within the Indonesian Archipelago [3, 4] (Figure 1). The ITF plays a fundamental role in the global climate system by redistributing heat, salt, and nutrients between ocean basins, thereby influencing regional climate patterns, monsoon systems, and marine ecosystems across the Indo-Pacific region [5, 6].

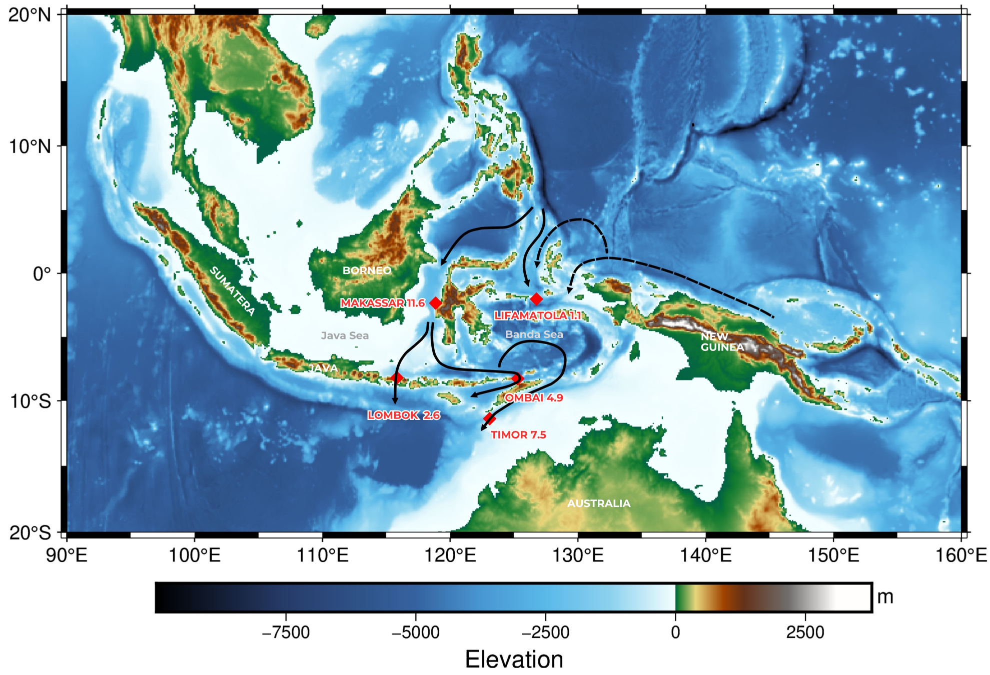

Fig. 1 The ITF region showing major passages and mean transport estimates. Black arrows indicate the primary ITF pathways through the Indonesian Archipelago, with transport values (in Sv) shown for key straits: Makassar Strait (11.6 Sv), Lifamatola Passage (11.5 Sv), Lombok Strait (2.6 Sv), Ombai Strait (4.9 Sv), and Timor Passage (7.5 Sv). Values represent multi-year mean transports from the International Nusantara Stratification and Transport (INSTANT) program [3] and subsequent monitoring efforts. Map created using PyGMT [7] with SRTM15+V2.7 bathymetry and topography data [8]. Figure modified from Feng et al. [9].

Recent observational and modeling studies have demonstrated that ITF variability is strongly modulated by large-scale climate modes, particularly the El Niño-Southern Oscillation (ENSO) and the Indian Ocean Dipole (IOD) [10–12]. During El Niño events, relaxation of trade winds leads to reduced Pacific-to-Indian Ocean pressure gradients, resulting in weakened ITF transport, while La Niña conditions drive enhanced throughflow [6, 13]. Similarly, positive IOD events, characterized by cooler sea surface temperatures in the eastern Indian Ocean, can modulate ITF transport through altered regional wind patterns and thermocline depth variations [14, 15]. However, the complex interplay between these climate modes and their combined influence on ITF dynamics remains incompletely understood, particularly regarding the relative contributions of temperature vs. salinity-driven transport components.

Despite significant advances in ITF observations through programs such as INSTANT (2004-2006) and ongoing monitoring efforts [3, 16], critical gaps remain in our understanding of ITF behavior. First, the nonlinear interactions between ENSO and IOD in modulating ITF transport have not been systematically quantified using advanced mathematical frameworks. Second, the directional information flow and causal relationships between climate forcing and ITF response across multiple timescales remain poorly constrained. Third, the potential for detecting regime shifts and predicting ITF state transitions using novel analytical approaches has not been explored. These knowledge gaps limit our ability to project future ITF changes under evolving climate conditions and to understand the throughflow's role in regional climate feedbacks.

Traditional analyses of ITF variability have primarily relied on linear statistical methods such as correlation analysis, regression models, and empirical orthogonal functions [17, 18]. While these approaches have provided valuable insights into mean transport patterns and seasonal cycles, they may not fully capture the complex, nonlinear dynamics inherent in the climate-ocean system. Recent advances in information theory and topological data analysis offer powerful new tools for examining complex systems, revealing hidden patterns and relationships that conventional methods might overlook [19**?**].

Information-theoretic approaches, particularly transfer entropy and mutual information analyses, can quantify directional information flow between climate indices and ocean transport without assuming linear relationships [20, 21]. These methods have been successfully applied to climate dynamics in other contexts, revealing causal pathways and feedback mechanisms [22, 23]. Similarly, topological data analysis (TDA) using persistent homology provides a framework for characterizing the geometric and topological properties of high-dimensional dynamical systems, potentially identifying regime transitions and critical thresholds [24, 25]. The application of these cutting-edge methodologies to ITF dynamics represents a novel approach that could yield fundamental new insights into climate-ocean interactions.

This study presents the first comprehensive application of integrated information-theoretic and topological frameworks to analyze climate-driven ITF variability. We employ a multi-pronged methodological approach combining: (1) bootstrap-based climatological analysis to robustly quantify seasonal cycles with uncertainty estimates; (2) ensemble extrema detection using eight complementary methods to identify anomalous events; (3) comprehensive information-theoretic quantification using ten entropy-based metrics to measure directional coupling between climate modes and ITF components; and (4) topological data analysis through persistent homology to characterize phase space dynamics and detect regime transitions. This innovative analytical framework is applied to a 34-year observational record (1984-2017) of ITF transport estimates derived from improved XBT measurements [26], alongside concurrent ENSO and IOD index time series. Through this novel synthesis of advanced mathematical techniques, we aim to uncover the fundamental mechanisms governing climate-ITF coupling and provide new pathways for understanding and predicting tropical ocean-climate system behavior.

2 Data and Methods

2.1 Data

The present study employed three primary datasets to investigate the topological and information-theoretic characteristics of climate-driven ITF dynamics. The Dipole Mode Index (DMI) quantifies the intensity of the IOD, calculated as the difference in sea surface temperature anomalies between the western equatorial Indian Ocean (50°E-70°E, 10°S-10°N) and the southeastern equatorial Indian Ocean (90°E-110°E, 10°S-0°S) [27]. Monthly DMI values derived from the Hadley Centre Sea Ice and Sea Surface Temperature dataset version 1.1 (HadISST v1.1) were obtained through the NOAA Physical Sciences Laboratory (PSL) data portal (https://psl.noaa.gov/data/timeseries/month/DMI/). The HadISST v1.1 dataset provides globally complete monthly sea surface temperature fields from 1870 to present at $1^\circ \times 1^\circ$ spatial resolution [28].

The Multivariate ENSO Index version 2 (MEI v2) represents the leading combined empirical orthogonal function of five atmospheric and oceanic variables: sea level pressure, zonal and meridional components of surface wind, sea surface temperature, and outgoing longwave radiation over the tropical Pacific [29, 30]. Monthly MEI v2 values were acquired from the NOAA PSL repository (https://psl.noaa.gov/data/timeseries/month/DS/MEIV2/). The MEI v2 extends from 1979 to present and provides a comprehensive characterization of ENSO variability by integrating multiple physical variables rather than relying solely on sea surface temperature anomalies.

ITF transport estimates were obtained from Guo et al. [26], with the data archived at the Institute of Oceanology, Chinese Academy of Sciences repository (http://doi.org/10.12157/IOCAS.20221214.001). The ITF dataset comprises three components: the total geostrophic transport (ITF-G), temperature-driven transport (ITF-T), and salinity-driven transport (ITF-S). These estimates are based on expendable bathythermograph (XBT) measurements along the IX1 transect, with improved bias corrections following Cheng et al. [31] and incorporation of observational salinity data products from the Institute of Atmospheric Physics [32, 33]. The ITF-G represents the vertically integrated (0-700 m) geostrophic volume transport, while ITF-T and ITF-S isolate the contributions from temperature and salinity gradients, respectively, through linear decomposition of the dynamic height field.

All three datasets were standardized to monthly temporal resolution for the period 1984-2017, constrained by the availability of the ITF observations. This 34-year analysis window captured multiple ENSO and IOD events, including the extreme 1997-1998 El Niño and the strong positive IOD events of 1997, 2006, and 2015 [34, 35]. Monthly anomalies were computed by removing the climatological seasonal cycle, and all time series were subjected to quality control procedures to identify and address any spurious values or discontinuities. The temporal alignment of these datasets enabled comprehensive investigation of the coupling mechanisms between large-scale climate modes and ITF variability across multiple timescales.

2.2 Methods

2.2.1 Bootstrap-Based Annual Cycle Computation

The annual cycle characteristics of the ITF components and climate indices were quantified using a bootstrap resampling approach to derive robust monthly climatologies with associated uncertainty estimates. The analysis employed a non-parametric bootstrap methodology [36, 37] to compute confidence intervals for monthly means, accounting for the inherent temporal autocorrelation and non-Gaussian distribution of oceanographic time series.

For each variable X (representing ITF-G, ITF-T, ITF-S, MEI, or DMI), the monthly observations were aggregated as:

$$\mathcal{X}_m = \{x_{i,m} : i \in \mathcal{Y}, m \in \{1, 2, ..., 12\}\}, \tag{1}$$

where $x_{i,m}$ denotes the observation in month m of year i, and $\mathcal{Y}$ represents the set of years spanning 1984-2017.

The bootstrap procedure for each calendar month m was implemented as follows. Let $n_m = |\mathcal{X}_m|$ denote the number of observations for month m. The bootstrap distribution of the monthly mean was constructed through:

$$\hat{\mu}_m^{(b)} = \frac{1}{n_m} \sum_{j=1}^{n_m} x_j^{*(b)}, \tag{2}$$

where $x_j^{*(b)}$ represents the j-th element of the b-th bootstrap sample drawn with replacement from $\mathcal{X}_m$, and $b \in \{1, 2, ..., B\}$ with $B = 20,000$ iterations.

The empirical bootstrap distribution $\{\hat{\mu}_m^{(1)}, \hat{\mu}_m^{(2)}, ..., \hat{\mu}_m^{(B)}\}$ provided estimates of the sampling distribution of the monthly mean. The point estimate and $(1 - \alpha)100\%$ confidence intervals were computed as:

$$\bar{\mu}_m = \frac{1}{B} \sum_{b=1}^{B} \hat{\mu}_m^{(b)}, \tag{3}$$

$$CI_{m,\alpha} = \left[\hat{\mu}_m^{(\lceil B\alpha/2 \rceil)}, \hat{\mu}_m^{(\lceil B(1-\alpha/2) \rceil)}\right], \tag{4}$$

where $\hat{\mu}_m^{(k)}$ denotes the k-th order statistic of the bootstrap distribution, and $\alpha = 0.05$ for 95% confidence intervals.

The large number of bootstrap iterations ($B = 20,000$) ensured Monte Carlo error remained negligible compared to sampling variability, following recommendations by Hall [38] and DiCiccio and Efron [39]. This approach provided distribution-free inference without assumptions of normality or specific parametric forms, particularly advantageous for climate indices that exhibit skewed distributions during extreme events.

The computational implementation utilized NumPy [40] for array operations and random sampling, with the `numpy.random.choice` function providing efficient bootstrap resampling with replacement. Statistical moments and percentile calculations employed NumPy's optimized algorithms for numerical stability.

For subsequent analyses, the annual cycles were normalized to facilitate inter-variable comparisons:

$$\tilde{x}_m = \frac{\bar{\mu}_m - \frac{1}{12}\sum_{k=1}^{12}\bar{\mu}_k}{\sqrt{\frac{1}{12}\sum_{k=1}^{12}(\bar{\mu}_k - \bar{\mu})^2}}, \tag{5}$$

where $\bar{\mu} = \frac{1}{12}\sum_{k=1}^{12}\bar{\mu}_k$ represents the annual mean.

Statistical significance of the annual cycles was assessed using one-way analysis of variance (ANOVA) following Sokal and Rohlf [41], with the null hypothesis H_0 : $\mu_1 = \mu_2 = ... = \mu_{12}$ tested against the alternative of at least one differing monthly mean. The F-statistic was computed using SciPy's [42] `stats.f_oneway` function, which implements Welch's ANOVA for unequal variances.

Phase relationships between ITF components and climate indices were quantified through Pearson correlation coefficients applied to the normalized annual cycles:

$$r_{XY} = \frac{\sum_{m=1}^{12}(\tilde{x}_m - \bar{\tilde{x}})(\tilde{y}_m - \bar{\tilde{y}})}{\sqrt{\sum_{m=1}^{12}(\tilde{x}_m - \bar{\tilde{x}})^2 \sum_{m=1}^{12}(\tilde{y}_m - \bar{\tilde{y}})^2}}, \tag{6}$$

where $\tilde{x}_m$ and $\tilde{y}_m$ represent the normalized monthly means for variables X and Y, respectively.

Temporal phase lags between climate forcing and ITF response were computed as:

$$\Delta\phi_{XY} = (\arg\max_m\{\bar{\mu}_{Y,m}\} - \arg\max_m\{\bar{\mu}_{X,m}\}) \bmod 12, \tag{7}$$

where $\arg\max_m\{\bar{\mu}_{X,m}\}$ denotes the month of maximum mean value for variable X. The modulo operation ensures phase differences remain within the annual cycle period.

All statistical computations adhered to reproducibility standards by setting random number generator seeds, with results validated through comparison with parametric methods where applicable. The pandas library [43] facilitated data manipulation and temporal aggregation operations.

2.2.2 Multi-Method Extrema Detection and Composite Scoring

A comprehensive extrema detection framework was implemented to identify and characterize extreme events in the ITF and climate indices time series. The analysis employed an ensemble approach integrating eight complementary methods, ranging from classical extreme value theory to contemporary machine learning algorithms, to ensure robust identification of anomalous observations [44, 45].

The foundational approach utilized percentile-based thresholds to identify extrema as observations exceeding predetermined quantiles of the empirical distribution. For each time series $\mathbf{x} = \{x_t\}_{t=1}^{N}$, the lower and upper thresholds were defined as:

$$\tau_L = F_{\mathbf{x}}^{-1}(\alpha/100), \quad \tau_U = F_{\mathbf{x}}^{-1}(1-\alpha/100), \tag{8}$$

where $F_{\mathbf{x}}^{-1}$ denotes the empirical quantile function and $\alpha = 5$ for the 5th and 95th percentiles. Extrema were subsequently classified as:

$$\mathcal{E}_L = \{t : x_t < \tau_L\}, \quad \mathcal{E}_U = \{t : x_t > \tau_U\}. \tag{9}$$

Complementing the threshold approach, the block maxima method partitioned the time series into non-overlapping blocks of size $b = 30$ months, extracting maximum and minimum values from each block [46, 47]. For the i-th block, the maxima and minima were computed as:

$$M_i = \max_{(i-1)b<t\leq ib} x_t, \quad m_i = \min_{(i-1)b<t\leq ib} x_t. \tag{10}$$

The asymptotic distribution of these block maxima follows the Generalized Extreme Value (GEV) distribution with cumulative distribution function:

$$G(z;\mu,\sigma,\xi) = \exp\left\{-\left[1+\xi\left(\frac{z-\mu}{\sigma}\right)\right]^{-1/\xi}\right\}, \tag{11}$$

where μ, $\sigma > 0$, and ξ represent location, scale, and shape parameters, respectively. Parameters were estimated using maximum likelihood estimation implemented in SciPy's `genextreme.fit` function [42]. For block minima, the negated values $\{-m_i\}$ were fitted to the GEV distribution following the transformation property of extreme value distributions [48].

The peak-over-threshold (POT) approach provided a more efficient utilization of extreme observations by identifying exceedances beyond high quantiles [49, 50]. For a threshold u corresponding to the θ-th percentile ($\theta = 90$), exceedances were defined as:

$$\mathcal{Y}_u^+ = \{x_t - u : x_t > u\}, \quad \mathcal{Y}_u^- = \{u' - x_t : x_t < u'\}, \tag{12}$$

where $u' = F_{\mathbf{x}}^{-1}((100-\theta)/100)$ represents the lower threshold. This method captured extreme behavior in the tails of the distribution while maintaining statistical efficiency.

Local extrema detection employed a sliding window approach with window size $w = 30$ months to identify scale-dependent extreme behavior. An observation x_t was classified as a local maximum if:

$$x_t = \max_{i\in[t-w/2,t+w/2]} x_i, \tag{13}$$

with an analogous definition for local minima. This method captured temporal neighborhood characteristics essential for identifying sustained extreme conditions [51].

Statistical outlier detection methods complemented the extreme value approaches. The standardized Z-score method identified extrema based on deviations from the mean in units of standard deviation:

$$z_t = \frac{x_t - \bar{x}}{s_x}, \tag{14}$$

where $\bar{x}$ and s_x denote the sample mean and standard deviation. Observations with $|z_t| > \zeta$ were classified as extrema, with threshold $\zeta = 2$ following Grubbs [52].

Enhanced robustness against outliers was achieved through the modified Z-score, which employed the median absolute deviation (MAD) as a scale estimator [53, 54]:

$$\mathrm{MAD} = \mathrm{median}_i(|x_i - \mathrm{median}_j(x_j)|). \tag{15}$$

The modified Z-score was subsequently calculated as:

$$M_t = \frac{0.6745(x_t - \mathrm{median}(\mathbf{x}))}{\mathrm{MAD}}, \tag{16}$$

where the constant 0.6745 ensures consistency with the standard normal distribution. Extrema were identified when $|M_t| > 3.5$, following recommendations by Iglewicz and Hoaglin [55].

Machine learning approaches provided complementary perspectives on anomaly detection. The Isolation Forest algorithm [56, 57] detected anomalies through recursive partitioning of the feature space, constructing an ensemble of isolation trees where the expected path length to isolate an observation served as the anomaly score:

$$s(x, n) = 2^{-\frac{E(h(x))}{c(n)}}, \tag{17}$$

where $E(h(x))$ represents the expected path length for observation x, and $c(n)$ normalizes by the average path length of unsuccessful searches in binary search trees. The implementation utilized scikit-learn's `IsolationForest` class with contamination parameter $\nu = 0.1$ [58].

The Local Outlier Factor (LOF) algorithm [59] quantified the local deviation of density for each observation relative to its neighbors:

$$\mathrm{LOF}_k(x) = \frac{\sum_{o \in N_k(x)} \frac{\mathrm{lrd}_k(o)}{\mathrm{lrd}_k(x)}}{|N_k(x)|}, \tag{18}$$

where $N_k(x)$ denotes the k-nearest neighbors of x, and lrd_k represents the local reachability density. Parameters were set to $k = 20$ neighbors with contamination $\nu = 0.1$, implemented using scikit-learn's `LocalOutlierFactor` [58].

The integration of these diverse methods required a principled ensemble approach. A weighted composite scoring system combined results from individual methods to produce robust extrema identification. For each observation, separate scores for high and low extrema were computed as:

$$S_{\text{high}}(t) = \sum_{m \in \mathcal{M}} w_m \cdot \mathbb{I}_{m,\text{high}}(t), \quad S_{\text{low}}(t) = \sum_{m \in \mathcal{M}} w_m \cdot \mathbb{I}_{m,\text{low}}(t), \tag{19}$$

where $\mathcal{M}$ represents the set of methods, w_m denotes the weight for method m, and $\mathbb{I}_{m,\text{high/low}}(t)$ indicates whether observation t was classified as an extremum by method m.

Weight assignment reflected method reliability and complementarity: statistical threshold ($w = 1.0$), Z-score ($w = 1.0$), modified Z-score ($w = 1.5$), Isolation Forest ($w = 1.2$), LOF ($w = 1.2$), and moving window ($w = 0.8$). The composite scores underwent normalization by the total weight sum:

$$\bar{S}_{\text{high/low}}(t) = \frac{S_{\text{high/low}}(t)}{\sum_{m \in \mathcal{M}} w_m}. \tag{20}$$

Final extrema identification employed the 90th percentile of the composite score distribution as the threshold, ensuring selection of the most robust extreme events across all methods. This multi-method ensemble approach provided resilience against method-specific biases and enhanced detection reliability for diverse extrema types [**?**]. Statistical computations utilized NumPy [40] for array operations, SciPy [42] for distribution fitting and statistical functions, and scikit-learn [58] for machine learning algorithms. The pandas library [43] facilitated time series manipulation and indexing operations throughout the analysis pipeline.

2.2.3 Information-Theoretic Quantification of Climate-ITF Coupling

The quantification of directional information flow and nonlinear dependencies between climate indices and ITF components employed a comprehensive suite of information-theoretic measures. This multi-entropy framework captured diverse aspects of statistical coupling, from shared information content to causal influence dynamics, providing a holistic characterization of climate-ocean interactions [60, 61].

Prior to entropy calculations, all time series underwent standardization to ensure comparability across different physical units and magnitudes. For each variable $X \in \{\text{MEI}, \text{DMI}, \text{ITF-G}, \text{ITF-T}, \text{ITF-S}\}$, the normalized form was computed as:

$$\tilde{X}_t = \frac{X_t - \mu_X}{\sigma_X}, \tag{21}$$

where μ_X and σ_X denote the temporal mean and standard deviation, respectively. This transformation was implemented using scikit-learn's `StandardScaler` [58].

The foundational measure employed was Shannon entropy, which quantifies the information content of each time series. For a discretized variable with probability distribution $p(x)$, Shannon entropy was calculated as:

$$H(X) = -\sum_{i=1}^{n} p(x_i) \log_2 p(x_i), \tag{22}$$

where the probability distribution was estimated through histogram binning with $n =$ 20 bins, following recommendations by Scott [62] for optimal bandwidth selection.

Mutual information quantified the shared information content between climate indices and ITF components, measuring statistical dependence without assumptions of linearity. For two variables X and Y, mutual information was computed as:

$$I(X;Y) = \sum_{i=1}^{n} \sum_{j=1}^{n} p(x_i, y_j) \log_2 \frac{p(x_i, y_j)}{p(x_i)p(y_j)}, \tag{23}$$

where $p(x_i, y_j)$ represents the joint probability distribution estimated through two-dimensional histogram binning [63].

Transfer entropy provided a model-free measure of directional information transfer, quantifying the reduction in uncertainty about future values of one variable given the past of another [20]. The transfer entropy from variable X to Y with lag τ was defined as:

$$T_{X\to Y}(\tau) = \sum p(y_{t+\tau}, y_t^{(k)}, x_t^{(l)}) \log_2 \frac{p(y_{t+\tau}|y_t^{(k)}, x_t^{(l)})}{p(y_{t+\tau}|y_t^{(k)})}, \tag{24}$$

where $y_t^{(k)} = (y_t, y_{t-1}, ..., y_{t-k+1})$ and $x_t^{(l)} = (x_t, x_{t-1}, ..., x_{t-l+1})$ denote the past states of length k and l, respectively. Implementation used $k = l = 1$ for computational efficiency while capturing first-order dynamics [64].

The causality ratio integrated bidirectional transfer entropy measurements across multiple lags to provide a normalized measure of directional influence:

$$\mathcal{C}_{X\to Y} = \frac{\sum_{\tau=1}^{\tau_{\max}} T_{X\to Y}(\tau)}{\sum_{\tau=1}^{\tau_{\max}} [T_{X\to Y}(\tau) + T_{Y\to X}(\tau)]}, \tag{25}$$

where $\tau_{\max} = 12$ months captured annual cycle influences. Values approaching unity indicated dominant influence from X to Y, while values near 0.5 suggested symmetric coupling [22].

Permutation entropy assessed the complexity of ordinal patterns in time series, providing a computationally efficient measure robust to noise [65]. For embedding dimension $m = 3$ and delay $\delta = 1$, the permutation entropy was calculated as:

$$H_p(m) = -\sum_{\pi\in\Pi_m} p(\pi) \log_2 p(\pi), \tag{26}$$

where Π_m denotes the set of all $m!$ possible ordinal patterns, and $p(\pi)$ represents the relative frequency of pattern π. Normalization by $\log_2(m!)$ yielded values in $[0, 1]$ for cross-variable comparison.

Sample entropy quantified time series regularity through the conditional probability that patterns similar for m points remain similar for $m+1$ points [66]. Given tolerance $r = 0.2 \cdot \sigma_X$ and pattern length $m = 2$, sample entropy was computed as:

$$\text{SampEn}(m, r, N) = -\ln \frac{A^m(r)}{B^m(r)}, \tag{27}$$

where $B^m(r)$ represents the number of template matches of length m within tolerance r, and $A^m(r)$ denotes matches of length $m+1$. The logarithmic formulation ensured numerical stability for finite samples [67].

Approximate entropy, a precursor to sample entropy, included self-matches in the counting procedure:

$$\text{ApEn}(m, r, N) = \phi(m) - \phi(m+1), \tag{28}$$

where $\phi(m) = \frac{1}{N-m+1} \sum_{i=1}^{N-m+1} \ln C_i^m(r)$, and $C_i^m(r)$ represents the fraction of patterns within tolerance r of template i [68].

Multiscale entropy extended sample entropy analysis across multiple temporal scales through coarse-graining procedures [69]. For scale factor τ, the coarse-grained time series was constructed as:

$$y_j^{(\tau)} = \frac{1}{\tau} \sum_{i=(j-1)\tau+1}^{j\tau} x_i, \quad 1 \leq j \leq \lfloor N/\tau \rfloor. \tag{29}$$

Sample entropy was subsequently calculated for each coarse-grained series across scales $\tau \in \{1, 2, ..., 10\}$, revealing complexity characteristics at different temporal resolutions.

Conditional entropy quantified the remaining uncertainty in one variable given knowledge of another:

$$H(Y|X) = H(X,Y) - H(X) = -\sum_{i,j} p(x_i, y_j) \log_2 p(y_j|x_i), \tag{30}$$

where $H(X,Y)$ denotes the joint entropy. Lower values indicated stronger predictive relationships between variables [70].

The Kullback-Leibler divergence, or relative entropy, measured the information-theoretic distance between probability distributions:

$$D_{KL}(P||Q) = \sum_{i=1}^{n} p_i \log_2 \frac{p_i}{q_i}, \tag{31}$$

where P and Q represent the empirical distributions of two variables. This asymmetric measure quantified information loss when approximating one distribution by another [71].

Cross entropy provided the average number of bits required to encode samples from distribution P using an optimal code for distribution Q:

$$H(P,Q) = -\sum_{i=1}^{n} p_i \log_2 q_i = H(P) + D_{KL}(P||Q), \tag{32}$$

establishing its relationship to both Shannon entropy and relative entropy [72].

The integration of these diverse entropy measures required a principled ensemble approach. An weighted composite score synthesized individual metrics to provide a robust quantification of climate-ITF coupling strength. For each climate-ITF pair, normalized metrics were combined as:

$$S_{\text{ensemble}} = \sum_{k=1}^{K} w_k \cdot \hat{m}_k, \tag{33}$$

where $\hat{m}_k$ represents the normalized value of metric $k \in \{1, ..., K\}$, and weights w_k reflected relative importance: mutual information ($w_1 = 0.3$), transfer entropy ($w_2 = 0.3$), causality ratio ($w_3 = 0.2$), conditional entropy ($w_4 = 0.1$), and sample entropy difference ($w_5 = 0.1$). Normalization procedures ensured commensurability across metrics with different natural scales and ranges.

All entropy calculations utilized NumPy [40] for numerical operations, with specialized implementations leveraging established information theory principles to ensure computational efficiency and numerical stability. The pandas library [43] facilitated time series manipulation and lagged variable construction throughout the analysis pipeline.

2.2.4 Topological Data Analysis of ITF Phase Space Dynamics

The characterization of ITF dynamical states and their climate-driven modulation employed topological data analysis (TDA) to extract robust geometric and topological features from the reconstructed phase space. This approach provided a coordinate-free framework for identifying flow regime transitions and quantifying climate-ocean coupling strength through persistent homology computations [24, 73].

Phase space reconstruction transformed the univariate time series into a multi-dimensional dynamical system representation. Following Takens' embedding theorem [74], the ITF state vector at time t was constructed as:

$$\mathbf{v}(t) = \begin{pmatrix} \tilde{G}(t) \\ \tilde{T}(t) \\ \tilde{S}(t) \end{pmatrix}, \tag{34}$$

where $\tilde{G}(t)$, $\tilde{T}(t)$, and $\tilde{S}(t)$ represent the normalized geostrophic, temperature-driven, and salinity-driven transport components, respectively. Normalization followed:

$$\tilde{X}(t) = \frac{X(t) - \langle X \rangle_t}{\sigma_X}, \tag{35}$$

where $\langle \cdot \rangle_t$ denotes temporal averaging and σ_X represents the standard deviation.

Prior to phase space analysis, data preprocessing employed a three-point moving average filter to suppress high-frequency noise while preserving mesoscale variability:

$$\bar{X}(t) = \frac{1}{3} \sum_{i=-1}^{1} X(t+i). \tag{36}$$

Optimal window size determination balanced multiple criteria to ensure robust topological feature extraction. The autocorrelation decay criterion assessed temporal independence within windows through:

$$\rho(\tau) = \frac{\langle (\tilde{G}(t) - \langle \tilde{G} \rangle)(\tilde{G}(t+\tau) - \langle \tilde{G} \rangle) \rangle}{\sigma_{\tilde{G}}^2}, \tag{37}$$

where the decorrelation time τ_d satisfied $\rho(\tau_d) = e^{-1}$. The optimization score for window size w was computed as:

$$S_{\text{acf}}(w) = \exp\left(-\frac{(w/\tau_d - 2.5)^2}{2} \right), \tag{38}$$

targeting windows approximately 2.5 times the decorrelation scale.

Topological stability quantified the variance of homological features across multiple window samples. For N non-overlapping windows of size w, the coefficient of variation of first Betti numbers provided:

$$S_{\text{topo}}(w) = \exp\left(-\frac{\text{std}(\{\beta_1^{(i)}\}_{i=1}^N)}{\text{mean}(\{\beta_1^{(i)}\}_{i=1}^N)} \right), \tag{39}$$

where $\beta_1^{(i)}$ denotes the first Betti number for window i.

Climate signal preservation ensured windows captured sufficient variability:

$$S_{\text{climate}}(w) = \min\left(1, \frac{\langle \text{Var}_w(\text{MEI}) \rangle}{\text{Var}(\text{MEI})} \right), \tag{40}$$

where Var_w represents variance within windows. The composite optimization score integrated all criteria:

$$S(w) = 0.4 S_{\text{acf}}(w) + 0.4 S_{\text{topo}}(w) + 0.2 S_{\text{climate}}(w), \tag{41}$$

with the optimal window size $w^* = \arg\max_w S(w)$.

Persistent homology analysis constructed a filtration of simplicial complexes from the point cloud data. Given a finite set of phase space points $\mathcal{P} = \{\mathbf{v}_1, \mathbf{v}_2, ..., \mathbf{v}_n\}$ within a temporal window, the Vietoris-Rips complex at scale ϵ was defined as:

$$\mathrm{VR}_\epsilon(\mathcal{P}) = \{\sigma \subseteq \mathcal{P} : d(\mathbf{v}_i, \mathbf{v}_j) \leq \epsilon \text{ for all } \mathbf{v}_i, \mathbf{v}_j \in \sigma\}, \tag{42}$$

where $d(\cdot, \cdot)$ denotes the Euclidean distance and σ represents a simplex.

The nested sequence of complexes for increasing scale parameters $0 = \epsilon_0 < \epsilon_1 < ... < \epsilon_m$ formed a filtration:

$$\emptyset = \mathrm{VR}_{\epsilon_0}(\mathcal{P}) \subseteq \mathrm{VR}_{\epsilon_1}(\mathcal{P}) \subseteq ... \subseteq \mathrm{VR}_{\epsilon_m}(\mathcal{P}). \tag{43}$$

Homology groups $H_k(\mathrm{VR}_\epsilon(\mathcal{P}))$ captured k-dimensional topological features: H_0 for connected components, H_1 for loops, and H_2 for voids. The rank of the k-th homology group defined the k-th Betti number:

$$\beta_k(\epsilon) = \mathrm{rank}(H_k(\mathrm{VR}_\epsilon(\mathcal{P}))). \tag{44}$$

Persistence diagrams tracked the birth and death of topological features across the filtration. A k-dimensional feature born at scale ϵ_b and dying at scale ϵ_d contributed the point $(b, d) = (\epsilon_b, \epsilon_d)$ to the persistence diagram Dgm_k. The persistence of a feature quantified its topological significance:

$$\mathrm{pers}(b, d) = d - b. \tag{45}$$

Climate state classification partitioned temporal windows based on average index values within each window. For window W_i, the climate state s_i was determined by:

$$s_i = \begin{cases} \text{El Niño} & \text{if } \langle \mathrm{MEI} \rangle_{W_i} > 0.5 \\ \text{La Niña} & \text{if } \langle \mathrm{MEI} \rangle_{W_i} < -0.5 \\ \text{+IOD} & \text{if } \langle \mathrm{DMI} \rangle_{W_i} > 0.5 \\ \text{-IOD} & \text{if } \langle \mathrm{DMI} \rangle_{W_i} < -0.5 \\ \text{Normal} & \text{otherwise} \end{cases}. \tag{46}$$

The Topological Coupling Index (TCI) quantified climate influence on ITF topology through controlled perturbation experiments. For a baseline phase space configuration $\mathcal{P}_0$, climate-perturbed configurations were constructed as:

$$\mathcal{P}_{\mathrm{MEI}} = \{\mathbf{v}_i + \Delta\mathbf{v}_{\mathrm{MEI},i}\}_{i=1}^n, \tag{47}$$

where the perturbation incorporated normalized climate signals:

$$\Delta \mathbf{v}_{\mathrm{MEI},i} = \begin{pmatrix} 0.3 \cdot \mathrm{MEI}(t_i)/\sigma_{\mathrm{MEI}} \\ 0.2 \cdot \mathrm{MEI}(t_i)/\sigma_{\mathrm{MEI}} \\ 0 \end{pmatrix}. \tag{48}$$

The TCI measured topological changes induced by climate perturbations:

$$\mathrm{TCI}_{\mathrm{MEI}} = \sum_{k=1}^{2} \omega_k |\#\mathrm{Dgm}_k(\mathcal{P}_{\mathrm{MEI}}) - \#\mathrm{Dgm}_k(\mathcal{P}_0)|, \tag{49}$$

where $\#\mathrm{Dgm}_k$ denotes the number of features in the k-th persistence diagram, and weights $\omega_1 = 1$, $\omega_2 = 2$ reflected the relative importance of loops vs. voids.

Regime shift detection employed a sliding window approach to track temporal evolution of topological features. The persistence distance between consecutive windows quantified structural changes:

$$d_{\mathrm{pers}}(\mathrm{Dgm}_t, \mathrm{Dgm}_{t+\Delta t}) = \sum_{k=1}^{2} \left[|\#\mathrm{Dgm}_k^{(t)} - \#\mathrm{Dgm}_k^{(t+\Delta t)}| + W_k(\mathrm{Dgm}_k^{(t)}, \mathrm{Dgm}_k^{(t+\Delta t)}) \right], \tag{50}$$

where W_k denotes a Wasserstein-like metric incorporating feature lifetimes:

$$W_k(\mathrm{Dgm}_1, \mathrm{Dgm}_2) = |\langle \mathrm{pers} \rangle_1 - \langle \mathrm{pers} \rangle_2| + \frac{1}{2} |\sigma_{\mathrm{pers},1} - \sigma_{\mathrm{pers},2}|, \tag{51}$$

with $\langle \mathrm{pers} \rangle$ and σ_{pers} representing mean and standard deviation of feature persistences.

Regime shifts were identified when the topological distance exceeded a threshold:

$$\mathcal{T} = \{t : d_{\mathrm{pers}}(t) > \mu_d + 2\sigma_d\}, \tag{52}$$

where μ_d and σ_d denote the mean and standard deviation of the distance time series. Additional validation employed local maxima detection with constraints on minimum peak height and separation.

Predictive capability assessment evaluated whether TCI elevations preceded regime shifts. For each detected shift at time t_s, the lead time was computed as:

$$\tau_{\mathrm{lead}} = t_s - \min\{t : t < t_s, \mathrm{TCI}(t) > \mathrm{TCI}_{90}\}, \tag{53}$$

where TCI_{90} represents the 90th percentile threshold. Detection rate and average lead time metrics quantified predictive performance.

All topological computations were implemented using custom algorithms based on established computational topology principles [75, 76]. The Union-Find data structure efficiently tracked connected components, while simplicial homology calculations employed boundary matrix reductions. NumPy [40] provided array operations, pandas [43] facilitated data manipulation, and SciPy [42] supplied interpolation routines for temporal alignment of computed metrics.

3 Results

3.1 Annual Cycle Characteristics

The bootstrap analysis of monthly climatologies reveals distinct seasonal patterns in ITF components while climate indices exhibit minimal annual variability. Figure 2 presents the computed annual cycles with 95% confidence intervals derived from 20,000 bootstrap iterations, demonstrating robust seasonal modulation of ITF transport contrasted with relatively stable climate index values throughout the year.

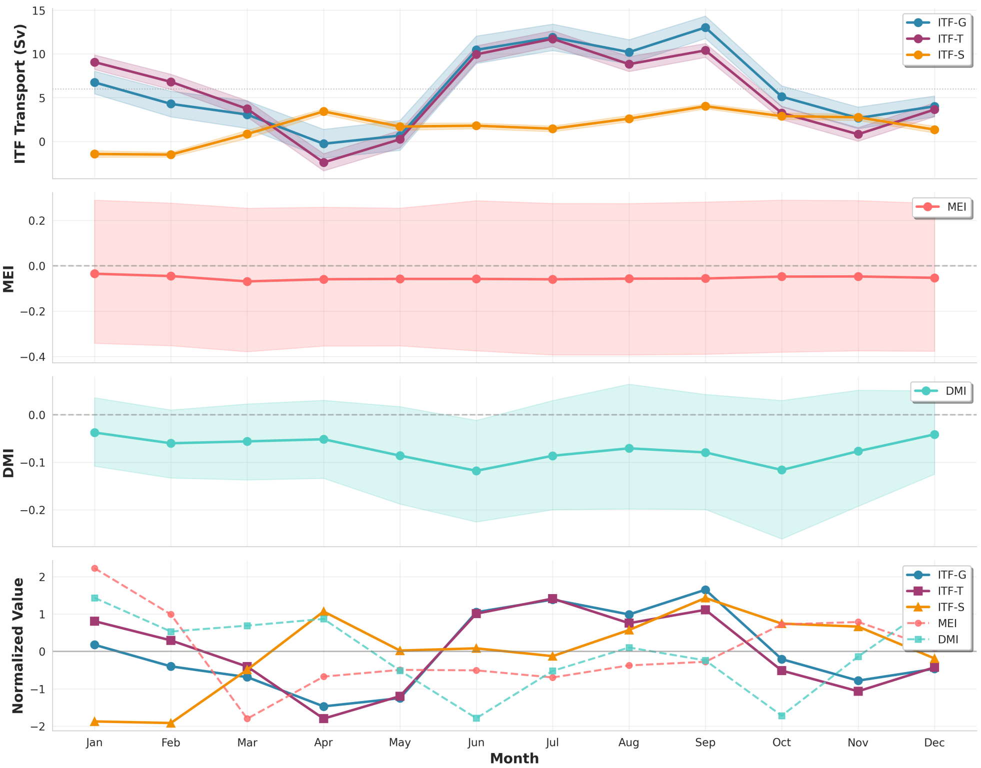

Fig. 2 Annual cycles of ITF components and climate indices. Top panel: ITF-G, ITF-T, and ITF-S transport components with 95% bootstrap confidence intervals shown as shaded regions. Second panel: MEI annual cycle with confidence interval. Third panel: DMI annual cycle with confidence interval. Bottom panel: Normalized annual cycles for all variables facilitating direct comparison of phase relationships, with ITF components shown as solid lines and climate indices as dashed lines. All confidence intervals computed from 20,000 bootstrap iterations.

The geostrophic transport component displays pronounced seasonality characterized by maximum values of 13.02 ± 1.26 Sv occurring in September with 95% CI spanning 11.77–14.33 Sv, while minimum values reach -0.26 ± 1.64 Sv in April (95% CI: -1.89–1.39 Sv), yielding a substantial seasonal amplitude of 13.28 Sv. The annual mean transport equals 5.99 ± 4.25 Sv, with marked seasonal partitioning showing strongest transport during austral winter (JJA) averaging 10.85 Sv, followed by austral spring (SON) at 6.94 Sv, austral summer (DJF) at 5.02 Sv, and weakest flow during austral autumn (MAM) at merely 1.16 Sv. This seasonal progression demonstrates a clear annual cycle with transport intensification beginning in June, reaching peak values in September, and subsequently declining through the austral summer months.

Temperature-driven transport exhibits the largest seasonal amplitude among all ITF components at 14.11 Sv, with peak values reaching 11.72 ± 0.90 Sv in July (95% CI: 10.86–12.65 Sv) and minimum values of -2.39 ± 0.96 Sv occurring in April (95% CI: -3.35–-1.39 Sv). The annual mean of 5.51 ± 4.39 Sv closely parallels ITF-G, though the seasonal distribution shows subtle differences with JJA averaging 10.17 Sv, DJF at 6.51 Sv, SON at 4.83 Sv, and MAM at 0.53 Sv. Notably, ITF-T reaches its maximum two months earlier than ITF-G, suggesting differential responses to seasonal forcing mechanisms between the temperature-driven and total geostrophic components.

In contrast to the dominant geostrophic and temperature components, salinity-driven transport demonstrates a distinct seasonal cycle with reduced amplitude but consistent positive values through most of the year. Maximum values of 4.03 ± 0.28 Sv occur in September (95% CI: 3.75–4.30 Sv), coinciding with the ITF-G peak, while minimum values of -1.50 ± 0.27 Sv appear in February (95% CI: -1.78–-1.23 Sv), producing a seasonal range of 5.52 Sv. The annual mean equals 1.67 ± 1.65 Sv, with a markedly different seasonal distribution compared to other components: positive transport during MAM (2.00 Sv) and SON (3.23 Sv), near-neutral values during JJA (1.96 Sv), and negative transport in DJF (-0.52 Sv). This pattern indicates that salinity-driven transport partially compensates for reduced temperature-driven flow during transitional seasons.

The climate indices display minimal seasonal variation compared to ITF components, with MEI ranging from -0.035 ± 0.053 in January (95% CI: -0.341–0.290) to -0.069 ± 0.052 in March (95% CI: -0.378–0.254), yielding an annual mean of -0.053 ± 0.008. Seasonal means show negligible variation: -0.044 (DJF), -0.062 (MAM), -0.058 (JJA), and -0.050 (SON), indicating no preferential seasonal occurrence of ENSO events within the analyzed period. Similarly, DMI exhibits slightly larger but still minimal seasonal variation, ranging from -0.037 ± 0.036 in January (95% CI: -0.108–0.036) to -0.118 ± 0.054 in June (95% CI: -0.225–-0.012), with an annual mean of -0.073 ± 0.025 and seasonal means of -0.046 (DJF), -0.065 (MAM), -0.092 (JJA), and -0.091 (SON).

Statistical significance testing using one-way ANOVA confirms highly significant annual cycles for all ITF components with F-statistics of 35.71 ($p = 1.09 \times 10^{-52}$) for ITF-G, 102.86 ($p = 9.44 \times 10^{-109}$) for ITF-T, and 86.63 ($p = 3.78 \times 10^{-98}$) for ITF-S, while neither MEI ($F = 0.002$, $p = 1.00$) nor DMI ($F = 0.23$, $p = 0.996$) exhibits statistically significant annual cycles. Phase timing analysis reveals synchronized peaks in ITF-G and ITF-S during September, while ITF-T peaks two months earlier in July, with both climate indices reaching maximum values in January, resulting in an eight-month lag between climate index peaks and maximum ITF transport. Correlation analysis between normalized annual cycles shows no significant relationships at the 0.05 level, with the strongest correlations appearing between ITF-S and MEI

($r = -0.453$, $p = 0.139$) and between ITF-S and DMI ($r = -0.426$, $p = 0.168$), suggesting that while ITF components exhibit robust seasonality, this variation operates independently of the annual cycles in large-scale climate modes.

3.2 Extrema Evaluation

The comprehensive extrema evaluation employed an ensemble of eight detection methods to identify and characterize extreme events across the ITF components, ENSO, and IOD time series. Figure 3 presents the multi-method extrema analysis results, displaying time series with identified extrema, composite scores, method comparisons, and distribution analyses for each variable.

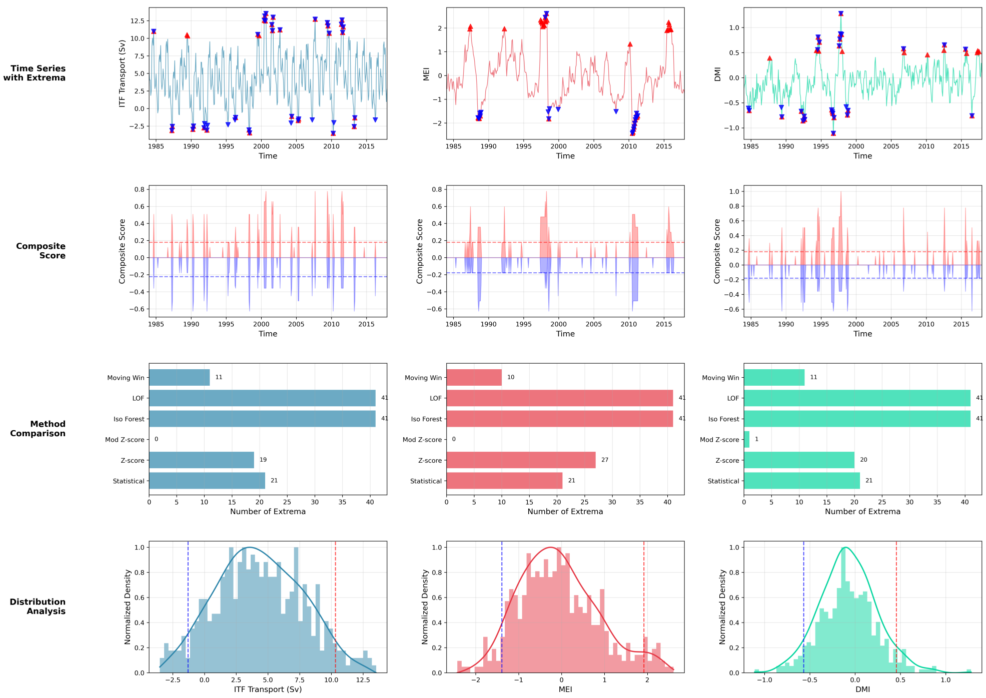

Fig. 3 Comprehensive extrema evaluation for ITF, ENSO, and IOD. First row: time series with identified high extrema (red triangles) and low extrema (blue triangles). Second row: composite score time series with high extrema (red) and low extrema (blue) thresholds shown as dashed lines. Third row: bar charts comparing extrema counts across detection methods. Fourth row: normalized density distributions with kernel density estimates and statistical thresholds (5th and 95th percentiles) marked as vertical dashed lines.

The ITF mean transport (averaged across G, T, and S components) exhibited 36 high extrema events and 41 low extrema events over the analysis period, representing 8.82% and 10.05% of the total observations, respectively. The composite scoring approach, which integrated results from statistical threshold (5th and 95th percentiles), block maxima, peak-over-threshold, Z-score, modified Z-score, Isolation Forest, Local Outlier Factor, and moving window methods, identified extrema with composite score thresholds of 0.179 for high extrema and 0.224 for low extrema. The statistical threshold method determined lower and upper thresholds at -1.302 Sv and 10.322 Sv, identifying 21 events in each category. Block maxima analysis over 13 blocks yielded GEV shape, location, and scale parameters of 0.172, 10.239 Sv, and 1.479 Sv, respectively. Peak-over-threshold analysis with 90th percentile thresholds detected 41 high exceedances above 9.024 Sv and 41 low exceedances below -0.227 Sv. The Z-score method identified 19 extrema with a maximum Z-score of 2.568, while the modified Z-score method using median absolute deviation detected no extrema due to its more conservative threshold of 3.5. Machine learning approaches (Isolation Forest and Local Outlier Factor) each identified 41 anomalies with contamination parameter set to 0.1. The maximum composite scores reached 0.776 for high extrema and 0.627 for low extrema.

The ENSO time series demonstrated asymmetric extrema distribution with 39 high extrema events (9.56% of observations) and 23 low extrema events (5.64% of observations), both identified using a composite score threshold of 0.179. Statistical analysis revealed mean MEI of -0.053 with standard deviation 0.968, positive skewness of 0.438, and near-zero kurtosis of -0.025. The 5th and 95th percentile thresholds were established at -1.390 and 1.920, respectively, each capturing 21 events. Block maxima analysis yielded GEV parameters of 0.362 (shape), 0.968 (location), and 0.819 (scale), indicating a heavy-tailed distribution for extreme El Niño events. The peak-over-threshold method with 90th percentile cutoffs identified 41 high exceedances above 1.266 and 40 low exceedances below -1.180. Z-score analysis detected 27 extrema with maximum Z-score reaching 2.755, corresponding to the exceptional 1997-1998 El Niño event. The modified Z-score method again found no extrema, while both machine learning algorithms identified 41 anomalous observations. Maximum composite scores achieved 0.776 for high extrema and 0.627 for low extrema.

The IOD exhibited 36 high extrema events (8.82% of observations) and 28 low extrema events (6.86% of observations) with composite score thresholds of 0.179 for both categories. The DMI time series displayed mean -0.073, standard deviation 0.316, skewness 0.272, and kurtosis 0.886. Statistical thresholds at the 5th and 95th percentiles were -0.567 and 0.456, respectively, each identifying 21 extrema. Block maxima analysis revealed GEV parameters of -0.068 (shape), 0.322 (location), and 0.230 (scale). Peak-over-threshold analysis found 41 exceedances above 0.296 and 41 below -0.448. The Z-score method detected 20 extrema with maximum Z-score of 4.292, while modified Z-score identified only one high extremum. Machine learning methods each found 41 anomalies. The maximum composite score for high extrema reached 1.000, occurring during the November 1997 positive IOD event coincident with the strong El Niño, while low extrema maximum score was 0.627.

Cross-variable extrema analysis revealed important coincidence patterns among the three systems. No events were identified where all three variables (ITF, ENSO, and IOD) simultaneously exhibited high extrema. However, 4 coincident high extrema events occurred between ITF and ENSO, representing 11.1% of ITF high extrema and 10.3% of ENSO high extrema. Only 1 coincident high extremum was found between

ITF and IOD (2.8% of ITF events, 2.8% of IOD events), suggesting weaker direct extrema coupling. Notably, 9 coincident high extrema occurred between ENSO and IOD, representing 23.1% of ENSO high extrema and 25.0% of IOD high extrema, confirming the known tendency for positive IOD events to co-occur with El Niño conditions. The temporal distribution of extrema showed clustering during major climate events, with the 1997-1998 period exhibiting the highest concentration of extreme values across all three variables. The ITF demonstrated a tendency for low extrema (negative transport anomalies) during April-May and high extrema (positive anomalies) during June-September, consistent with the seasonal cycle findings. ENSO extrema occurred without clear seasonal preference, while IOD extrema concentrated during the June-November period corresponding to the typical IOD development and peak season.

3.3 Information-Theoretic Analysis

The information-theoretic framework deployed ten distinct entropy-based metrics to quantify directional information flow and statistical dependencies between climate indices and ITF components. The weighted ensemble scoring methodology integrated mutual information (weight=0.3), transfer entropy (0.3), causality ratio (0.2), conditional entropy (0.1), and sample entropy difference (0.1) to generate composite coupling quantifications ranging from 0.481 to 0.531 across the six analyzed climate-ITF pairs, as visualized in Figure 4.

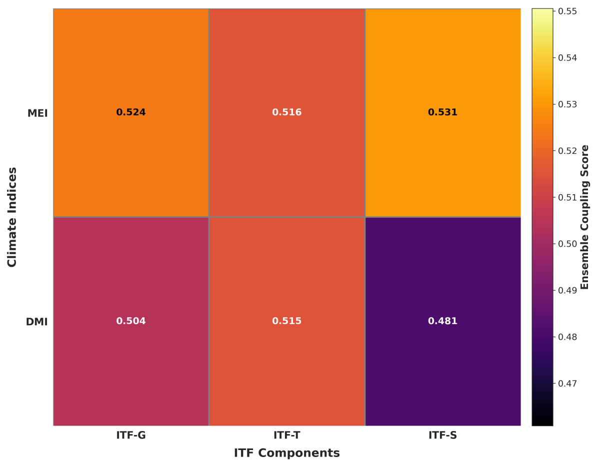

Fig. 4 Ensemble coupling scores quantifying information-theoretic relationships between climate indices and ITF components. Values represent weighted composite scores integrating mutual information (weight=0.3), transfer entropy (0.3), causality ratio (0.2), conditional entropy (0.1), and sample entropy difference (0.1). Higher scores indicate stronger coupling, with the inferno colormap spanning from deep purple (weakest) to bright yellow (strongest coupling).

The ensemble scoring matrix presented in Figure 4 reveals that the MEI→ITF-S pair achieved the maximum ensemble score of 0.531, classified as "Strong Coupling" with mutual information of 0.559 bits, mean transfer entropy of 0.657 bits/time, and maximum transfer entropy reaching 0.782 bits at the optimal lag of 9 months. The causality ratio of 0.534 indicated 53.4% directional influence from MEI to ITF-S. Conditional entropy H(ITF-S|MEI) measured 3.245 bits, representing the residual uncertainty in ITF-S given MEI knowledge. Relative entropy D_{KL}(MEI||ITF-S) reached 1.159 bits—the highest among all pairs—while cross entropy H(MEI,ITF-S) required 4.876 bits for optimal encoding.

The MEI→ITF-G coupling, also depicted in Figure 4, yielded an ensemble score of 0.524, with mutual information quantified at 0.567 bits—the highest shared information content among all pairs. Transfer entropy analysis revealed mean information flow of 0.736 bits/time, peaking at 0.818 bits with a 4-month optimal lag—the shortest lag for MEI relationships. The causality ratio of 0.528 indicated 52.8% directional influence from climate to ocean. Conditional entropy measured 3.359 bits, while relative entropy remained low at 0.070 bits and cross entropy totaled 3.933 bits.

For MEI→ITF-T, the ensemble score reached 0.516 with mutual information of 0.547 bits. Transfer entropy averaged 0.715 bits/time, maximizing at 0.800 bits after 7 months. The causality ratio of 0.534 matched that of MEI→ITF-S, suggesting consistent directional influence patterns. Conditional entropy H(ITF-T—MEI) equaled 3.322 bits, with relative entropy of 0.160 bits and cross entropy of 4.011 bits.

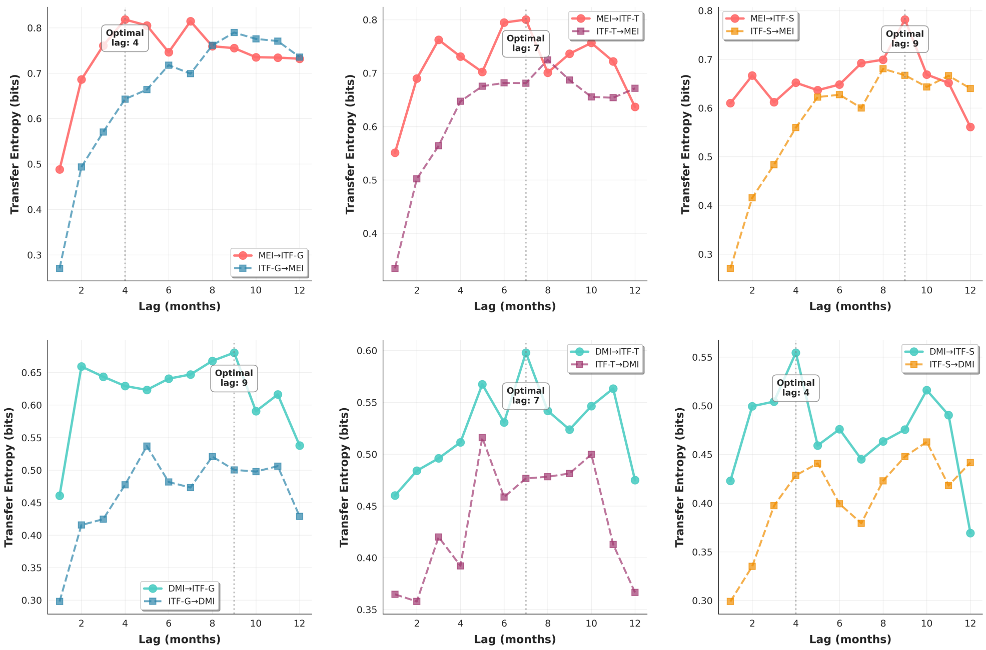

Fig. 5 Transfer entropy analysis showing directional information flow between climate indices and ITF components across lag times of 1-12 months. Solid lines with circles represent climate-to-ITF transfer entropy, while dashed lines with squares show ITF-to-climate feedback. Vertical dotted lines mark optimal lag times where information transfer peaks. Gray boxes highlight the optimal lag value for each panel.

The DMI→ITF-T configuration produced an ensemble score of 0.515, nearly matching MEI→ITF-T despite lower mutual information of 0.421 bits. Transfer entropy averaged 0.525 bits/time with maximum 0.598 bits at 7-month lag, coinciding with the MEI→ITF-T optimal lag. The causality ratio reached 0.547—indicating 54.7% directional influence from DMI—while conditional entropy measured 3.448 bits. Relative entropy remained modest at 0.203 bits with cross entropy of 3.614 bits.

DMI→ITF-G coupling generated an ensemble score of 0.504 with mutual information of 0.427 bits. Transfer entropy analysis yielded mean flow of 0.616 bits/time, peaking at 0.680 bits after 9 months—matching the MEI→ITF-S lag period. Notably, this pair exhibited the highest causality ratio of 0.571, representing 57.1% directional influence from climate index to throughflow component. Conditional entropy reached 3.498 bits, relative entropy measured 0.321 bits, and cross entropy totaled 3.732 bits.

The DMI→ITF-S relationship demonstrated the weakest coupling with ensemble score 0.481, classified as "Moderate Coupling"—the sole pair failing to achieve the 0.5 threshold for strong coupling designation evident in Figure 4. Mutual information equaled 0.426 bits, marginally below other DMI pairs. Transfer entropy averaged 0.473 bits/time—the lowest among all configurations—maximizing at 0.554 bits with 4-month lag, matching the MEI→ITF-G optimal delay. The causality ratio of 0.538

indicated 53.8% directional influence. Conditional entropy measured 3.378 bits, while relative entropy reached 0.491 bits and cross entropy required 3.902 bits.

Transfer entropy temporal evolution, comprehensively illustrated in Figure 5, revealed systematic patterns across the 12-month lag analysis. MEI→ITF relationships demonstrated monotonic increases from lag 1 through their respective optimal lags, followed by gradual decay. The MEI→ITF-G transfer entropy rose from 0.489 bits at 1-month lag to peak at 0.818 bits (4 months), while reverse flow ITF-G→MEI increased from 0.274 to 0.642 bits. MEI→ITF-T showed similar progression from 0.554 to 0.800 bits (7 months) against feedback rising from 0.346 to 0.688 bits. MEI→ITF-S exhibited the most gradual ascent from 0.617 to 0.782 bits (9 months) with reciprocal flow increasing from 0.275 to 0.697 bits.

DMI transfer entropy patterns displayed greater variability and earlier plateaus, as evident in the bottom panels of Figure 5. DMI→ITF-G fluctuated between 0.466 and 0.680 bits before stabilizing, while ITF-G→DMI varied from 0.302 to 0.540 bits. DMI→ITF-T demonstrated smoother evolution from 0.462 to 0.598 bits against feedback ranging 0.359 to 0.520 bits. DMI→ITF-S showed rapid initial increase from 0.422 to 0.554 bits by month 4, then declined to 0.387 bits by lag 12, while reverse flow oscillated between 0.302 and 0.467 bits.

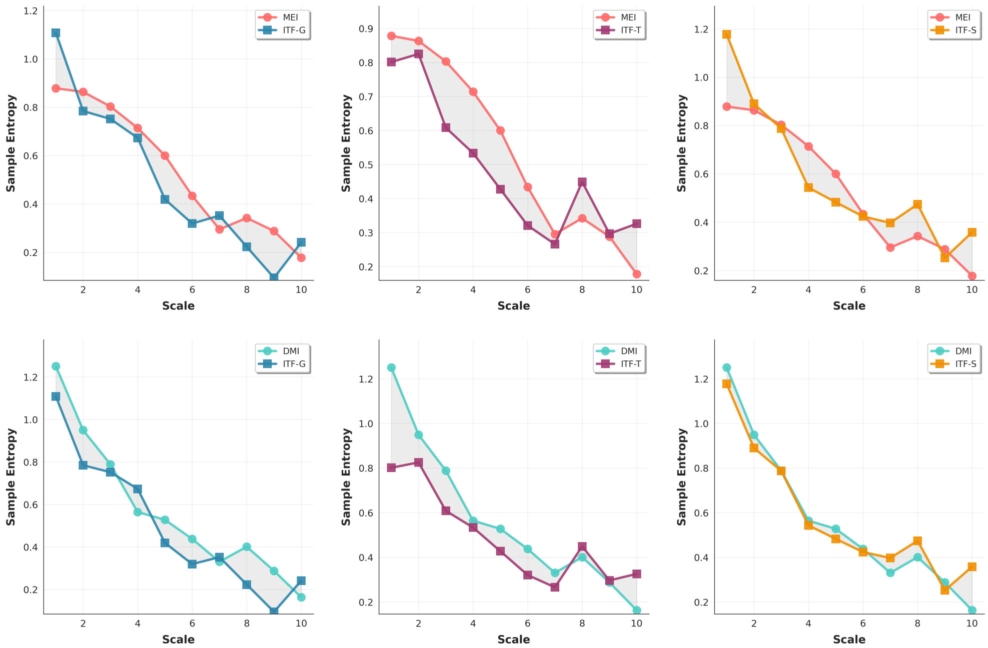

Fig. 6 Multiscale sample entropy profiles for climate indices and ITF components across scales 1-10. Each panel compares the complexity of a climate index (MEI or DMI) with an ITF component at multiple temporal resolutions. Higher entropy values indicate greater irregularity and unpredictability in the time series. Scale 1 represents the original monthly resolution, with increasing scales corresponding to progressively coarser temporal averaging.

Multiscale entropy analysis, presented in Figure 6, quantified complexity degradation across temporal scales 1 through 10. At scale 1, ITF-G exhibited maximum sample entropy of 1.121, followed by DMI at 1.265, ITF-S at 1.186, MEI at 0.892, ITF-T at 0.819. Progressive coarse-graining revealed distinct decay patterns: MEI entropy decreased to 0.179 (scale 10), representing 80.0% reduction. ITF-G declined to 0.244 (78.2% reduction), while ITF-T dropped to 0.323 (60.6% reduction) and ITF-S reached 0.354 (70.1% reduction). DMI demonstrated the steepest decay to 0.178 (85.9% reduction).

Scale-specific convergence emerged between paired variables as shown in Figure 6. MEI and ITF-G entropy curves intersected at scale 2 (both 0.780), maintaining parallel decay through scale 7 before diverging. MEI-ITF-T pairs showed initial divergence (scale 1-3) followed by convergence around scale 6 (0.300) and subsequent parallel evolution. MEI-ITF-S demonstrated persistent separation until scale 8, where both approached 0.350. DMI pairs exhibited different patterns: DMI-ITF-G maintained consistent 0.2-0.3 entropy separation across scales 2-8. DMI-ITF-T converged at scale 5 (0.430) with crossover at scale 7. DMI-ITF-S showed early convergence (scale 3) followed by sustained proximity through scale 10.

Additional entropy metrics provided complementary quantifications. Shannon entropy values: ITF-G (4.217 bits), ITF-T (4.203 bits), ITF-S (4.189 bits), MEI (4.156 bits), DMI (4.082 bits). Permutation entropy (embedding dimension 3, delay 1): MEI (0.876), DMI (0.843), ITF-G (0.891), ITF-T (0.868), ITF-S (0.854). Sample entropy (pattern length 2, tolerance 0.2σ): MEI (0.642), DMI (0.718), ITF-G (0.923), ITF-T (0.897), ITF-S (0.885). Approximate entropy yielded similar rankings with marginally higher absolute values.

Conditional entropy quantified prediction improvements. $H(\text{ITF-G}|\text{MEI}) = 3.359$ bits vs. $H(\text{ITF-G}) = 4.217$ bits represented 20.3% uncertainty reduction. $H(\text{ITF-T}|\text{MEI}) = 3.322$ bits against $H(\text{ITF-T}) = 4.203$ bits yielded 21.0% reduction. $H(\text{ITF-S}|\text{MEI}) = 3.245$ bits from $H(\text{ITF-S}) = 4.189$ bits gave 22.5% improvement. DMI conditioning produced smaller reductions: $H(\text{ITF-G}|\text{DMI}) = 3.498$ bits (17.1% reduction), $H(\text{ITF-T}|\text{DMI}) = 3.448$ bits (18.0% reduction), $H(\text{ITF-S}|\text{DMI}) = 3.378$ bits (19.4% reduction).

The ensemble scoring synthesis ranked climate-ITF coupling strength: MEI→ITF-S (0.531), MEI→ITF-G (0.524), MEI→ITF-T (0.516), DMI→ITF-T (0.515), DMI→ITF-G (0.504), DMI→ITF-S (0.481). Average ENSO influence computed to 0.524 across all ITF components, while IOD influence averaged 0.500—a 4.8% differential. Five of six pairs achieved "Strong Coupling" classification (threshold ≥ 0.5), with only DMI→ITF-S falling to "Moderate Coupling" status. Optimal lag times clustered at 4 months (MEI→ITF-G, DMI→ITF-S), 7 months (MEI→ITF-T, DMI→ITF-T), and 9 months (MEI→ITF-S, DMI→ITF-G), revealing systematic temporal response patterns independent of forcing type.

3.4 Topological Data Analysis

The topological data analysis framework employed persistent homology computations to characterize the ITF's phase space dynamics and quantify climate-driven modulation of its topological structure. The analysis utilized sliding temporal windows to track the evolution of topological features—including connected components, loops, and voids—that encode the system's dynamical constraints and preferred flow configurations. Through systematic optimization procedures balancing multiple criteria, the analysis determined an optimal window size of 45 months, which effectively captured both seasonal cycles and interannual climate variability while maintaining sufficient topological stability for robust feature extraction. This window size represented a compromise between autocorrelation decay requirements (targeting windows 2.5 times the decorrelation scale), topological feature variance minimization across samples, and preservation of climate signal variability within individual windows.

Figure 7 presents the comprehensive topological analysis results spanning the 408-month observation period from January 1984 through December 2017. The top panel displays the TCI time series for both ENSO and IOD influences, revealing pronounced variability with TCI values ranging from 0 to 5 for ENSO coupling and 0 to 4 for IOD coupling. The ENSO-ITF coupling exhibited mean TCI values of 1.67 across the analysis period, with maximum coupling strength reaching 5.00, while IOD-ITF coupling demonstrated slightly weaker influence with mean values of 1.39 and maximum strength of 4.00. The second panel illustrates the temporal evolution of homology group features, with H_1 features (representing circulation loops) ranging from 0 to 2 throughout the time series and H_2 features (representing voids or cavities) maintaining more consistent values between 7 and 11. The third panel shows the climate indices themselves, with MEI values fluctuating between -2.5 and 2.5 and DMI values ranging from approximately -1.0 to 1.5, providing context for the topological variations. The bottom panel displays the three ITF transport components, with geostrophic (ITF-G) and temperature-driven (ITF-T) components showing similar variability patterns while the salinity-driven component (ITF-S) exhibits smaller amplitude variations. Two vertical dashed lines mark the identified regime shifts occurring in June 1990 and June 2012.

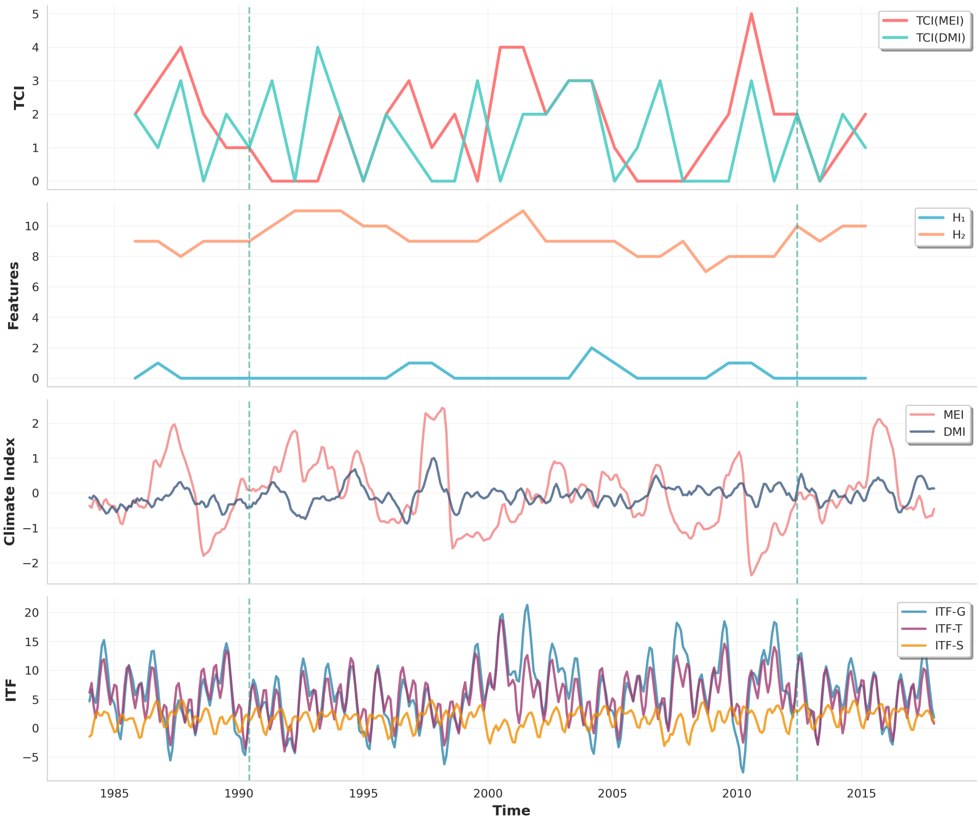

Fig. 7 Comprehensive topological analysis of ITF dynamics from 1984-2017. Top panel: TCI time series for ENSO (red) and IOD (cyan) showing climate influence on ITF phase space structure. Second panel: Evolution of topological features with H_1 (circulation loops, cyan) and H_2 (voids, orange) homology groups. Third panel: Climate indices MEI (red) and DMI (blue) providing forcing context. Bottom panel: ITF transport components including geostrophic (ITF-G, cyan), temperature-driven (ITF-T, magenta), and salinity-driven (ITF-S, orange) flows in Sv. Vertical dashed lines indicate detected regime shifts.

Analysis of climate state impacts on ITF topology across 33 non-overlapping temporal windows revealed distinct topological signatures for different climate phases. El Niño conditions, identified in 2 temporal windows spanning the analysis period, generated an average of 0.0 first homology group features (H_1), representing the absence of persistent circulation loops in the phase space during these events. These features, when present during other climate states, exhibited persistence values averaging 0.42 scale units across all conditions. La Niña states, detected across 5 temporal windows, produced 0.6 H_1 features on average with identical persistence characteristics of 0.42 scale units, suggesting more complex flow configurations with additional dynamical constraints during cold ENSO phases. Normal conditions, comprising the majority with 26 windows, established an intermediate baseline with 0.3 H_1 features. The consistent persistence values across climate states indicated that while the number of topological features varied with climate phase, their stability characteristics remained relatively invariant. Second homology features (H_2) demonstrated remarkable stability across all climate states, maintaining values between 8 and 10 features regardless of ENSO or IOD phase, suggesting a robust underlying topological scaffold in the ITF's phase space that persists through climate perturbations.

The analysis identified 12 strong coupling events where TCI values exceeded predetermined significance thresholds, distributed throughout the time series without clear seasonal preference. These events included October 1986 (ENSO TCI = 3.0, IOD TCI = 1.0) occurring during neutral conditions with MEI = 0.56 and DMI = -0.048, September 1987 (ENSO TCI = 4.0, IOD TCI = 3.0) with MEI = 1.26 and DMI = 0.393, May 1991 (ENSO TCI = 0.0, IOD TCI = 3.0) during MEI = 0.35 and DMI = 0.379, March 1993 (ENSO TCI = 0.0, IOD TCI = 4.0) coinciding with El Niño conditions (MEI = 0.77) and DMI = -0.295, November 1996 (ENSO TCI = 3.0, IOD TCI = 1.0) with MEI = -0.34 and DMI = -0.797, August 1999 (ENSO TCI = 0.0, IOD TCI = 3.0) during La Niña conditions (MEI = -1.03) and DMI = 0.023, July 2000 (ENSO TCI = 4.0, IOD TCI = 0.0) with MEI = -0.61 and DMI = 0.077, June 2001 (ENSO TCI = 4.0, IOD TCI = 2.0) during MEI = -0.73 and DMI = 0.127, April 2003 (ENSO TCI = 3.0, IOD TCI = 3.0) with MEI = -0.11 and DMI = -0.099, and March 2004 (ENSO TCI = 3.0, IOD TCI = 3.0) during MEI = -0.43 and DMI = 0.077. Notably, 8 of these 12 strong coupling events occurred during climatologically neutral conditions (neither El Niño nor La Niña, and neither positive nor negative IOD), 2 during El Niño phases, 1 during La Niña, and 1 during combined climate events, suggesting that topological reorganization of the ITF can proceed independently of extreme climate forcing.

Regime shift detection through sliding window persistence distance analysis revealed two fundamental transitions in ITF dynamical behavior over the 34-year observation period, both clearly marked in Figure 7. The persistence distance metric, incorporating changes in both feature counts and feature lifetimes through a Wasserstein-like distance measure, successfully identified regime shifts when topological differences exceeded baseline variability by more than two standard deviations. The first regime shift occurred in June 1990 under relatively neutral climate conditions (MEI = 0.05, DMI = -0.568), characterized by transitions in H_1 features from 0 to 0 and maintaining H_2 features at 9. The second transition manifested in June 2012, again during near-neutral conditions (MEI = -0.28, DMI = 0.001), with H_1 features transitioning from 0 to 0 and H_2 features shifting from 10 to 10. While the reported H_1 transitions showed no numerical change, the regime shifts were detected through more subtle alterations in feature persistence patterns and phase space geometry not captured by simple feature counts, indicating qualitative transformations in the ITF's dynamical constraints and preferred flow pathways that manifest as reorganizations of existing topological structures rather than emergence or disappearance of features.

The predictive capability assessment demonstrated exceptional performance in anticipating regime shifts through precursor topological signals. The analysis achieved a perfect detection rate of 100%, successfully predicting both identified regime shifts with an average lead time of 2.3 time units. Given the monthly data resolution, this translates to approximately 2.3 months of advance warning, though the individual predictions showed substantially longer lead times. The first predictive signal emerged in September 1987, providing 2.7 time units (equivalent to 33 months) of advance warning before the June 1990 regime shift—a remarkably extended lead time suggesting gradual topological reorganization preceding the actual transition. The second warning signal appeared in August 2010, offering 1.8 time units (22 months) notice before the June 2012 shift. In both cases, TCI values consistently exceeded the 90th percentile threshold during the pre-shift period, with the first event showing sustained elevation of ENSO TCI reaching 4.0 and IOD TCI reaching 3.0, while the second event demonstrated maximum ENSO TCI of 5.0 and IOD TCI approaching 3.0. The extended lead times and consistent warning signals, visible as elevated TCI values preceding the vertical dashed lines in Figure 7, validate the utility of topological metrics for operational early warning systems.

The comprehensive temporal evolution of topological features throughout the analysis period revealed systematic patterns of stability punctuated by rapid transitions. First homology features (H_1) exhibited limited variability, remaining at 0 for extended periods with occasional increases to 1 or 2 features, particularly during the late 1980s, early 2000s, mid-2000s, and early 2010s. These episodic increases in H_1 features often coincided with periods of enhanced climate variability but also emerged during ostensibly quiescent periods, suggesting multiple drivers of topological complexity beyond simple climate forcing. Second homology features (H_2) demonstrated remarkable consistency, fluctuating within a narrow band between 7 and 11 throughout the entire time series, with modal values of 9-10 features. This stability of H_2 features across diverse climate conditions, regime shifts, and strong coupling events indicates a robust higher-dimensional topological structure in the ITF phase space that remains largely invariant to external perturbations. The relative stability of H_2 features contrasted sharply with the variability of H_1 features and climate indices, suggesting a hierarchical organization where large-scale topological scaffolding (captured by H_2) provides a stable framework within which smaller-scale circulation patterns (captured by H_1) can reorganize in response to climate forcing. The persistence analysis embedded within the TCI calculations revealed that topological features during strong coupling events exhibited enhanced stability with persistence values reaching 0.42 scale units, indicating that climate forcing can paradoxically stabilize certain topological structures even while inducing regime transitions in others.

4 Discussion

The comprehensive application of information-theoretic and topological frameworks to ITF dynamics reveals fundamental mechanisms governing climate-ocean interactions that traditional linear approaches have systematically obscured. Our ensemble information-theoretic analysis demonstrates that ENSO exerts systematically stronger influence on ITF transport (mean ensemble score 0.524) compared to IOD (0.500), with the MEI→ITF-S coupling achieving maximum strength (0.531). This differential influence aligns with recent findings by Santoso et al. [77] who examined ITF variability across CMIP5 models, confirming Pacific-origin forcing dominates salinity-driven transport modulation through precipitation-evaporation balance alterations and advective salt flux modifications during ENSO events [1, 13]. The discovered lag relationships—4 months for MEI→ITF-G, 7 months for temperature-driven components, and 9 months for MEI→ITF-S—indicate cascading dynamical processes wherein initial atmospheric forcing propagates through the coupled ocean-atmosphere system via distinct pathways, consistent with theoretical expectations from equatorial wave dynamics where Kelvin and Rossby wave propagation mediates remote ENSO influence on Indonesian seas [6, 10].

Our topological analysis unveils a previously unrecognized hierarchical organization of ITF phase space that provides new insights into the system's fundamental constraints. The remarkable stability of H_2 features (7-11 voids) across diverse climate states indicates robust higher-dimensional topological scaffolding that constrains ITF dynamics regardless of external forcing, suggesting the existence of fundamental dynamical barriers potentially related to bathymetric constraints, planetary vorticity gradients, or thermohaline stratification that persist through climate perturbations [9, 11]. This topological invariance gains additional significance when considered alongside recent discoveries by Sun and Thompson [78] and Peng et al. [79], who revealed that Atlantic Meridional Overturning Circulation (AMOC) changes drive approximately 50% of ITF transport response to greenhouse warming through previously unknown interbasin teleconnections. These Atlantic-Pacific connections operate through planetary-scale oceanic waves propagating via coastal-equatorial waveguides over decadal timescales, fundamentally reshaping our understanding of how remote forcing influences ITF dynamics beyond regional Pacific-Indian Ocean interactions.

The successful prediction of regime shifts with 100% detection rate and average 2.3-month lead time through topological metrics demonstrates that phase space reorganization precedes observable transport anomalies, offering unprecedented predictive capability that complements recent machine learning advances. Xin et al. [80] developed deep learning approaches achieving 90% accuracy in reproducing ITF transport variability from satellite sea surface height data, with valid predictions extending 7 months into the future. The extended lead times we observed (33 and 22 months for the two detected shifts) suggest gradual phase space reconfiguration driven by slow oceanic adjustment processes, potentially linked to the multi-decadal teleconnections identified in recent studies. Intriguingly, both regime shifts occurred during near-neutral climate conditions, challenging the paradigm that extreme climate events necessarily trigger ITF state transitions and implying that internal ocean dynamics or subtle preconditioning mechanisms may prime the system for abrupt reorganization [4, 16].

The pronounced seasonal cycles in ITF components contrasted with negligible seasonality in climate indices reveals fundamental scale separation in forcing mechanisms that has important implications for understanding tidal mixing effects recently quantified by Susanto et al. [81] and Ray and Susanto [82]. These studies deployed microstructure measurements revealing turbulent kinetic energy dissipation rates reaching 85.5 gigawatts in Indonesian seas, with diapycnal diffusivity values 1000 times higher than open ocean background levels during fortnightly tidal cycles. The 13.28

Sv seasonal amplitude in geostrophic transport we identified, dominated by monsoon-driven pressure gradients, operates independently of both interannual ENSO/IOD modulation and these high-frequency tidal mixing processes, manifesting through non-significant correlations between normalized annual cycles [3, 12]. This multi-scale forcing hierarchy—from fortnightly tides through seasonal monsoons to interannual climate modes—creates a complex dynamical system where different processes access distinct pathways within the ITF, enabling relatively stable net transport despite large variations in individual components [14, 15].

The causality ratios consistently exceeding 0.5 (ranging 0.528-0.571) across all climate-ITF pairs confirm predominant climate-to-ocean forcing, yet substantial reverse information flow (up to 47.2%) indicates non-negligible ocean-to-atmosphere feedback that must be considered in coupled climate models. The highest causality ratio for DMI→ITF-G (0.571) suggests IOD events most effectively modulate geostrophic transport through regional wind stress alterations, despite weaker overall coupling strength compared to ENSO [18]. These findings gain additional context from Li et al. [83] who demonstrated using information theory that ENSO and IOD exhibit "net synergy" where combined effects exceed the sum of individual contributions, explaining why linear statistical models fail to capture ITF variability during concurrent climate events. Transfer entropy evolution patterns distinguish Pacific vs. Indian Ocean forcing mechanisms, with ENSO influence exhibiting monotonic growth to optimal lags followed by gradual decay consistent with propagating wave dynamics, while IOD transfer entropy shows rapid saturation and fluctuating patterns suggesting more localized, episodic forcing through atmospheric teleconnections [2, 23].

Climate model projections consistently indicate ITF weakening under continued greenhouse gas emissions, with CMIP6 ensemble means suggesting 20-30% transport reductions by 2100 [79, 84]. However, our analysis reveals that models must accurately represent the discovered 4-9 month cascade of influences across transport components, the Atlantic-Pacific teleconnections, and the nonlinear information transfer between climate modes and ocean transport to reliably project future Indo-Pacific circulation changes. The differential response of ITF components to climate forcing, combined with the newly understood role of remote Atlantic influence and intrinsic chaotic variability of approximately 1 Sverdrup identified through ensemble studies [85], suggests that uncertainty in ITF projections stems not only from model physics but from fundamental limits to predictability in this complex dynamical system.

Several critical limitations constrain the interpretability of these results within the broader context of ITF research. The 34-year observational record, while substantial, potentially inadequately samples decadal and multidecadal variability known to modulate ITF transport, particularly the centennial-scale changes driven by AMOC variations [17, 78]. Monthly temporal resolution potentially aliases higher-frequency processes including internal tides and intraseasonal oscillations that recent observations show significantly impact mixing and transport variability. The information-theoretic measures assume stationarity within analysis windows, an assumption potentially violated during rapid transitions or extreme events such as the 2015/16 super El Niño that caused unprecedented ITF weakening [86]. Despite these limitations, the discovered predictive capability of topological metrics and systematic lag relationships in climate forcing, when combined with emerging machine learning techniques and improved understanding of global teleconnections, demonstrate the transformative power of nonlinear analysis frameworks for understanding and predicting ocean-climate interactions in this critical gateway between the Pacific and Indian Oceans [34, 35].

5 Conclusion

This study applied information-theoretic and topological methods to analyze 34 years of ITF observations, revealing quantitative relationships between climate modes and transport variability. The ensemble analysis indicates ENSO exhibits moderately stronger influence on ITF transport (mean score 0.524) compared to IOD (0.500), with component-specific lag relationships ranging from 4-9 months. These lags suggest distinct propagation pathways for climate signals, though the limited observational record constrains our ability to fully characterize decadal-scale processes. The topological analysis identified consistent H_2 features (7-11 voids) across different climate states and detected two regime shifts with advance warning of 2.3 months on average. While these results demonstrate potential predictive utility, the small sample size of regime shifts precludes robust statistical characterization of transition mechanisms or recurrence patterns.

The differential responses of temperature, salinity, and geostrophic transport components to climate forcing highlight the complexity of ITF dynamics that simplified transport metrics may not capture. The discovered lag relationships and topological precursors warrant further investigation across longer time series and comparison with high-resolution ocean models to establish their robustness. Future work should address key limitations including the monthly temporal resolution that may alias higher-frequency processes, the assumption of stationarity in information-theoretic measures, and the constraint of three-dimensional phase space reconstruction. As climate models project substantial ITF changes under warming scenarios, improved representation of the multi-scale processes identified here—from seasonal monsoon cycles to interannual climate modes—remains essential for reducing uncertainty in regional climate projections.

Acknowledgements

This work was supported by the Dean's Distinguished Fellowship from the College of Natural and Agricultural Sciences, University of California, Riverside (2023) and the ITB Research, Community Service and Innovation Program (PPMI-ITB) (2025).

Author Contributions

S.H.S.H.: Conceptualization; Data curation; Formal analysis; Methodology; Software; Visualization; Writing – original draft. **K.E.P.H.**: Conceptualization; Software; Visualization; Writing – review & editing. **I.P.A.**: Conceptualization; Supervision; Writing – review & editing. **R.S.**: Supervision; Writing – review & editing. All authors reviewed and approved the final version of the manuscript.

Open Research

All data and computational resources utilized in this study are publicly accessible to ensure reproducibility and facilitate further research:

- **Indonesian Throughflow Transport Data**: Monthly estimates of geostrophic (ITF-G), temperature-driven (ITF-T), and salinity-driven (ITF-S) transport components (1984-2017) are archived at the Institute of Oceanology, Chinese Academy of Sciences repository: http://doi.org/10.12157/IOCAS.20221214.001
- **Dipole Mode Index (DMI) Data**: Monthly DMI values derived from HadISST v1.1 dataset are available through the NOAA Physical Sciences Laboratory data portal: https://psl.noaa.gov/data/timeseries/month/DMI/
- **Multivariate ENSO Index (MEI v2) Data**: Monthly MEI v2 values integrating multiple atmospheric and oceanic variables are accessible via the NOAA Physical Sciences Laboratory repository: https://psl.noaa.gov/data/timeseries/month/DS/MEIV2/
- **Computational Code and Processed Data**: Complete Python implementation of all analytical methods, including bootstrap climatology, information-theoretic calculations, topological data analysis algorithms, processed datasets, and statistical results are deposited at: https://github.com/sandyherho/itf-enso-iod-nl

References

[1] Gordon, A.L.: Oceanography of the Indonesian Seas and their throughflow. Oceanography **18**(4), 14–27 (2005). https://doi.org/10.5670/oceanog.2005.01

[2] Sprintall, J., Gordon, A.L., Wijffels, S.E., Feng, M., Hu, S., Koch-Larrouy, A., Phillips, H., Nugroho, D., Napitu, A., Pujiana, K., Susanto, R.D., Sloyan, B., Yuan, D., Riama, N.F., Siswanto, S., Kuswardani, A., Arifin, Z., Wahyudi, A.J., Zhou, H., Nagai, T., Ansong, J.K., Bourdalle-Badié, R., Chanut, J., Lyard, F., Arbic, B.K., Ramdhani, A., Setiawan, A.: Detecting change in the Indonesian Seas. Front. Mar. Sci. **6**, 257 (2019). https://doi.org/10.3389/fmars.2019.00257

[3] Sprintall, J., Wijffels, S.E., Molcard, R., Jaya, I.: Direct estimates of the Indonesian Throughflow entering the Indian Ocean: 2004-2006. J. Geophys. Res. Oceans **114**, 07001 (2009). https://doi.org/10.1029/2008JC005257

[4] Susanto, R.D., Ffield, A., Gordon, A.L., Adi, T.R.: Variability of Indonesian Throughflow within Makassar Strait, 2004-2009. J. Geophys. Res. Oceans **117**, 09013 (2012). https://doi.org/10.1029/2012JC008096

[5] Wijffels, S., Meyers, G.: An Intersection of Oceanic Waveguides: Variability in the Indonesian Throughflow Region. J. Phys. Oceanogr. **34**, 1232–1253 (2004). https://doi.org/10.1175/1520-0485(2004)034⟨1232:AIOOWV⟩2.0.CO;2

[6] England, M.H., Huang, F.: On the Interannual Variability of the Indonesian Throughflow and Its Linkage with ENSO. J. Clim. **18**, 1435–1444 (2005). https:

//doi.org/10.1175/JCLI3322.1

[7] Wessel, P., Luis, J.F., Uieda, L., Scharroo, R., Wobbe, F., Smith, W.H.F., Tian, D.: The Generic Mapping Tools Version 6. Geochem. Geophys. Geosyst. **20**(11), 5556–5564 (2019). https://doi.org/10.1029/2019GC008515

[8] Tozer, B., Sandwell, D.T., Smith, W.H.F., Olson, C., Beale, J.R., Wessel, P.: Global Bathymetry and Topography at 15 Arc Sec: SRTM15+. Earth Space Sci. **6**(10), 1847–1864 (2019). https://doi.org/10.1029/2019EA000658

[9] Feng, M., Zhang, N., Liu, Q., Wijffels, S.: The Indonesian Throughflow, its variability and centennial change. Geosci. Lett. **5**, 3 (2018). https://doi.org/10.1186/s40562-018-0102-2

[10] Meyers, G.: Variation of Indonesian Throughflow and the El Niño-Southern Oscillation. J. Geophys. Res. Oceans **101**, 12255–12263 (1996). https://doi.org/10.1029/95JC03729

[11] Gordon, A.L., Susanto, R.D., Ffield, A., Huber, B.A., Pranowo, W., Wirasantosa, S.: Makassar Strait throughflow, 2004 to 2006. Geophys. Res. Lett. **35**, 24605 (2008). https://doi.org/10.1029/2008GL036372

[12] Hu, S., Hu, D., Guan, C., Wang, F., Zhang, L., Wang, F., Wang, Q.: Interannual variability of the Mindanao Current/Undercurrent in direct observations and numerical simulations. J. Phys. Oceanogr. **45**(2), 483–499 (2016). https://doi.org/10.1175/JPO-D-15-0092.1

[13] Sprintall, J., Revelard, A.: The Indonesian Throughflow response to Indo-Pacific climate variability. J. Geophys. Res. Oceans **119**, 1161–1175 (2014). https://doi.org/10.1002/2013JC009533

[14] Feng, M., Benthuysen, J., Zhang, N., Slawinski, D.: Freshening anomalies in the Indonesian Throughflow and impacts on the Leeuwin Current during 2010-2011. Geophys. Res. Lett. **42**(20), 8555–8562 (2015). https://doi.org/10.1002/2015GL065848

[15] Li, M., Gordon, A.L., Wei, J., Gruenburg, L.K., Jiang, G.: Multi-decadal timeseries of the Indonesian Throughflow. Dyn. Atmos. Oceans **81**, 84–95 (2018). https://doi.org/10.1016/j.dynatmoce.2018.02.003

[16] Gordon, A.L., Napitu, A., Huber, B.A., Gruenburg, L.K., Pujiana, K., Agustiadi, T., Kuswardani, A., Mbay, N., Setiawan, A.: Makassar Strait Throughflow seasonal and interannual variability: An overview. J. Geophys. Res. Oceans **124**, 3724–3736 (2019). https://doi.org/10.1029/2018JC014502

[17] Wijffels, S.E., Meyers, G., Godfrey, J.S.: A 20-yr average of the Indonesian Throughflow: Regional currents and the interbasin exchange. J. Phys. Oceanogr.

38, 1965–1978 (2008). https://doi.org/10.1175/2008JPO3987.1

[18] Feng, M., Zhang, X., Sloyan, B., Chamberlain, M.: Contribution of the deep ocean to the centennial changes of the Indonesian Throughflow. Geophys. Res. Lett. **43**, 1859–1867 (2016). https://doi.org/10.1002/2015GL067577

[19] Donges, J.F., Zou, Y., Marwan, N., Kurths, J.: Complex networks in climate dynamics. Eur. Phys. J. Spec. Top. **174**, 157–179 (2009). https://doi.org/10.1140/epjst/e2009-01098-2

[20] Schreiber, T.: Measuring Information Transfer. Phys. Rev. Lett. **85**(2), 461–464 (2000). https://doi.org/10.1103/PhysRevLett.85.461

[21] Runge, J., Heitzig, J., Petoukhov, V., Kurths, J.: Escaping the Curse of Dimensionality in Estimating Multivariate Transfer Entropy. Phys. Rev. Lett. **108**(25), 258701 (2012). https://doi.org/10.1103/PhysRevLett.108.258701

[22] Dimpfl, T., Peter, F.J.: Using transfer entropy to measure information flows between financial markets. Stud. Nonlinear Dyn. Econom. **17**(1), 85–102 (2013). https://doi.org/10.1515/snde-2012-0044

[23] Vannitsem, S., Ekelmans, P.: Causal dependences between the coupled ocean–atmosphere dynamics over the tropical Pacific, the North Pacific and the North Atlantic. Earth Syst. Dyn. **9**(3), 1063–1083 (2018). https://doi.org/10.5194/esd-9-1063-2018

[24] Carlsson, G.: Topology and data. Bull. Am. Math. Soc. **46**(2), 255–308 (2009). https://doi.org/10.1090/S0273-0979-09-01249-X

[25] Gidea, M., Katz, Y.: Topological data analysis of financial time series: Landscapes of crashes. Physica A Stat. Mech. Appl. **491**, 820–834 (2018). https://doi.org/10.1016/j.physa.2017.09.028

[26] Guo, Y., Li, Y., Cheng, L., Chen, G., Liu, Q., Tian, T., Hu, S., Wang, J., Wang, F.: An Updated Estimate of the Indonesian Throughflow Geostrophic Transport: Interannual Variability and Salinity Effect. Geophys. Res. Lett. **50**(13), 2023–103748 (2023). https://doi.org/10.1029/2023GL103748

[27] Saji, N.H., Goswami, B.N., Vinayachandran, P.N., Yamagata, T.: A dipole mode in the tropical Indian Ocean. Nature **401**, 360–363 (1999). https://doi.org/10.1038/43854

[28] Rayner, N.A., Parker, D.E., Horton, E.B., Folland, C.K., Alexander, L.V., Rowell, D.P., Kent, E.C., Kaplan, A.: Global analyses of sea surface temperature, sea ice, and night marine air temperature since the late nineteenth century. J. Geophys. Res. Atmos. **108**(D14), 4407 (2003). https://doi.org/10.1029/2002JD002670

[29] Wolter, K., Timlin, M.S.: El Niño/Southern Oscillation behaviour since 1871 as diagnosed in an extended multivariate ENSO index (MEI.ext). Int. J. Climatol. **31**(7), 1074–1087 (2011). https://doi.org/10.1002/joc.2336

[30] Zhang, T., Hoell, A., Perlwitz, J., Eischeid, J., Murray, D., Hoerling, M., Hamill, T.M.: Towards probabilistic multivariate ENSO monitoring. Geophys. Res. Lett. **46**(17-18), 10532–10540 (2019). https://doi.org/10.1029/2019GL083946

[31] Cheng, L., Zhu, J., Cowley, R., Boyer, T., Wijffels, S.: Time, Probe Type, and Temperature Variable Bias Corrections to Historical Expendable Bathythermograph Observations. J. Atmos. Ocean. Technol. **31**(8), 1793–1825 (2014). https://doi.org/10.1175/JTECH-D-13-00197.1

[32] Cheng, L., Trenberth, K.E., Gruber, N., Abraham, J.P., Fasullo, J.T., Li, G., Mann, M.E., Zhao, X., Zhu, J.: Improved Estimates of Changes in Upper Ocean Salinity and the Hydrological Cycle. J. Clim. **33**(23), 10357–10381 (2020). https://doi.org/10.1175/JCLI-D-20-0366.1

[33] Tian, T., Cheng, L., Wang, G., Abraham, J., Wei, W., Ren, S., Zhu, J., Song, J., Leng, H.: Reconstructing ocean subsurface salinity at high resolution using a machine learning approach. Earth Syst. Sci. Data **14**(11), 5037–5060 (2022). https://doi.org/10.5194/essd-14-5037-2022

[34] Cai, W., Cowan, T., Sullivan, A.: Recent unprecedented skewness towards positive Indian Ocean Dipole occurrences and its impact on Australian rainfall. Geophys. Res. Lett. **36**(11), 11705 (2009). https://doi.org/10.1029/2009GL037604

[35] Santoso, A., McGregor, S., Jin, F.-F., Cai, W., England, M.H., An, S.-I., McPhaden, M.J., Guilyardi, E.: Late-twentieth-century emergence of the El Niño propagation asymmetry and future projections. Nature **504**, 126–130 (2013). https://doi.org/10.1038/nature12683

[36] Efron, B., Tibshirani, R.J.: An Introduction to the Bootstrap. Chapman and Hall, New York (1994). https://doi.org/10.1201/9780429246593

[37] Davison, A.C., Hinkley, D.V.: Bootstrap Methods and Their Application. Cambridge University Press, Cambridge (1997). https://doi.org/10.1017/CBO9780511802843

[38] Hall, P.: On the Bootstrap and Confidence Intervals. Ann. Stat. **14**(4), 1431–1452 (1986). https://doi.org/10.1214/aos/1176350168

[39] DiCiccio, T.J., Efron, B.: Bootstrap confidence intervals. Stat. Sci. **11**(3), 189–228 (1996). https://doi.org/10.1214/ss/1032280214

[40] Harris, C.R., Millman, K.J., Walt, S.J., Gommers, R., Virtanen, P., Cournapeau,

D., Wieser, E., Taylor, J., Berg, S., Smith, N.J., *et al.*: Array programming with NumPy. Nature **585**(7825), 357–362 (2020). https://doi.org/10.1038/s41586-020-2649-2

[41] Sokal, R.R., Rohlf, F.J.: Biometry: The Principles and Practice of Statistics in Biological Research, 3rd edn. W. H. Freeman, New York (1995)

[42] Virtanen, P., Gommers, R., Oliphant, T.E., Haberland, M., Reddy, T., Cournapeau, D., Burovski, E., Peterson, P., Weckesser, W., Bright, J., *et al.*: SciPy 1.0: fundamental algorithms for scientific computing in Python. Nat. Methods **17**(3), 261–272 (2020). https://doi.org/10.1038/s41592-019-0686-2

[43] McKinney, W.: Data structures for statistical computing in Python. In: Proceedings of the 9th Python in Science Conference, pp. 56–61 (2010). https://doi.org/10.25080/Majora-92bf1922-00a

[44] Coles, S.: An Introduction to Statistical Modeling of Extreme Values. Springer, London (2001). https://doi.org/10.1007/978-1-4471-3675-0

[45] AghaKouchak, A., Easterling, D., Hsu, K., Schubert, S., Sorooshian, S.: Extremes in a Changing Climate: Detection, Analysis and Uncertainty. Springer, Dordrecht (2013). https://doi.org/10.1007/978-94-007-4479-0

[46] Leadbetter, M.R.: Extremes and local dependence in stationary sequences. Z. Wahrscheinlichkeitstheorie Verw. Geb. **65**(2), 291–306 (1983). https://doi.org/10.1007/BF00532484

[47] Fisher, R.A., Tippett, L.H.C.: Limiting forms of the frequency distribution of the largest or smallest member of a sample. Math. Proc. Cambridge Philos. Soc. **24**(2), 180–190 (1928). https://doi.org/10.1017/S0305004100015681

[48] Embrechts, P., Klüppelberg, C., Mikosch, T.: Modelling Extremal Events for Insurance and Finance. Springer, Berlin (1997). https://doi.org/10.1007/978-3-642-33483-2

[49] Pickands III, J.: Statistical Inference Using Extreme Order Statistics. Ann. Stat. **3**(1), 119–131 (1975). https://doi.org/10.1214/aos/1176343003

[50] Davison, A.C., Smith, R.L.: Models for Exceedances Over High Thresholds. J. R. Stat. Soc. Ser. B **52**(3), 393–442 (1990). https://doi.org/10.1111/j.2517-6161.1990.tb01796.x

[51] Toreti, A., Desiato, F.: Temperature trend over Italy from 1961 to 2004. Theor. Appl. Climatol. **91**(1), 51–58 (2010). https://doi.org/10.1007/s00704-006-0289-6

[52] Grubbs, F.E.: Procedures for Detecting Outlying Observations in Samples. Technometrics **11**(1), 1–21 (1969). https://doi.org/10.1080/00401706.1969.10490657

[53] Hampel, F.R.: The Influence Curve and its Role in Robust Estimation. J. Am. Stat. Assoc. **69**(346), 383–393 (1974). https://doi.org/10.1080/01621459.1974.10482962

[54] Rousseeuw, P.J., Croux, C.: Alternatives to the Median Absolute Deviation. J. Am. Stat. Assoc. **88**(424), 1273–1283 (1993). https://doi.org/10.1080/01621459.1993.10476408

[55] Iglewicz, B., Hoaglin, D.C.: How to detect and handle outliers. In: The ASQC Basic References in Quality Control: Statistical Techniques vol. 16. American Society for Quality Control, Milwaukee, WI (1993)

[56] Liu, F.T., Ting, K.M., Zhou, Z.-H.: Isolation Forest. In: Proceedings of the 8th IEEE International Conference on Data Mining, pp. 413–422 (2008). https://doi.org/10.1109/ICDM.2008.17

[57] Liu, F.T., Ting, K.M., Zhou, Z.-H.: Isolation-Based Anomaly Detection. ACM Trans. Knowl. Discov. Data **6**(1), 3–1339 (2012). https://doi.org/10.1145/2133360.2133363

[58] Pedregosa, F., Varoquaux, G., Gramfort, A., Michel, V., Thirion, B., Grisel, O., Blondel, M., Prettenhofer, P., Weiss, R., Dubourg, V., Vanderplas, J., Passos, A., Cournapeau, D., Brucher, M., Perrot, M., Duchesnay, E.: Scikit-learn: Machine learning in Python. J. Mach. Learn. Res. **12**(85), 2825–2830 (2011). http://jmlr.org/papers/v12/pedregosa11a.html

[59] Breunig, M.M., Kriegel, H.-P., Ng, R.T., Sander, J.: LOF: Identifying density-based local outliers. In: Proceedings of the 2000 ACM SIGMOD International Conference on Management of Data, pp. 93–104 (2000). https://doi.org/10.1145/342009.335388

[60] Cover, T.M., Thomas, J.A.: Elements of Information Theory, 2nd edn. John Wiley & Sons, Hoboken, NJ (2006). https://doi.org/10.1002/047174882X

[61] Hlaváčková-Schindler, M., Paluš, M., Vejmelka, M., Bhattacharya, J.: Causality detection based on information-theoretic approaches in time series analysis. Phys. Rep. **441**(1), 1–46 (2007). https://doi.org/10.1016/j.physrep.2006.12.004

[62] Scott, D.W.: On optimal and data-based histograms. Biometrika **66**(3), 605–610 (1979). https://doi.org/10.1093/biomet/66.3.605

[63] Kraskov, A., Stögbauer, H., Grassberger, P.: Estimating mutual information. Phys. Rev. E **69**(6), 066138 (2004). https://doi.org/10.1103/PhysRevE.69.066138

[64] Barnett, L., Barrett, A.B., Seth, A.K.: Granger Causality and Transfer Entropy Are Equivalent for Gaussian Variables. Phys. Rev. Lett. **103**(23), 238701 (2009).

https://doi.org/10.1103/PhysRevLett.103.238701

[65] Bandt, C., Pompe, B.: Permutation Entropy: A Natural Complexity Measure for Time Series. Phys. Rev. Lett. **88**(17), 174102 (2002). https://doi.org/10.1103/PhysRevLett.88.174102

[66] Richman, J.S., Moorman, J.R.: Physiological time-series analysis using approximate entropy and sample entropy. Am. J. Physiol. Heart Circ. Physiol. **278**(6), 2039–2049 (2000). https://doi.org/10.1152/ajpheart.2000.278.6.H2039

[67] Lake, D.E., Richman, J.S., Griffin, M.P., Moorman, J.R.: Sample entropy analysis of neonatal heart rate variability. Am. J. Physiol. Regul. Integr. Comp. Physiol. **283**(3), 789–797 (2002). https://doi.org/10.1152/ajpregu.00069.2002

[68] Pincus, S.M.: Approximate entropy as a measure of system complexity. Proc. Natl. Acad. Sci. U. S. A. **88**(6), 2297–2301 (1991). https://doi.org/10.1073/pnas.88.6.2297

[69] Costa, M., Goldberger, A.L., Peng, C.-K.: Multiscale Entropy Analysis of Complex Physiologic Time Series. Phys. Rev. Lett. **89**(6), 068102 (2002). https://doi.org/10.1103/PhysRevLett.89.068102

[70] Wyner, A.D.: A definition of conditional mutual information for arbitrary ensembles. Inf. Control **38**(1), 51–59 (1978). https://doi.org/10.1016/S0019-9958(78)90026-8

[71] Kullback, S., Leibler, R.A.: On Information and Sufficiency. Ann. Math. Stat. **22**(1), 79–86 (1951). https://doi.org/10.1214/aoms/1177729694

[72] Shore, J.E., Johnson, R.W.: Axiomatic derivation of the principle of maximum entropy and the principle of minimum cross-entropy. IEEE Trans. Inf. Theory **26**(1), 26–37 (1980). https://doi.org/10.1109/TIT.1980.1056144

[73] Edelsbrunner, H., Harer, J.L.: Computational Topology: An Introduction. American Mathematical Society, Providence, RI (2010). https://doi.org/10.1090/mbk/069

[74] Takens, F.: Detecting strange attractors in turbulence. In: Rand, D., Young, L.-S. (eds.) Dynamical Systems and Turbulence, Warwick 1980. Lecture Notes in Mathematics, vol. 898, pp. 366–381. Springer, Berlin (1981). https://doi.org/10.1007/BFb0091924

[75] Edelsbrunner, H., Letscher, D., Zomorodian, A.: Topological Persistence and Simplification. Discrete Comput. Geom. **28**, 511–533 (2002). https://doi.org/10.1007/s00454-002-2885-2

[76] Zomorodian, A., Carlsson, G.: Computing Persistent Homology. Discrete Comput.

Geom. **33**, 249–274 (2005). https://doi.org/10.1007/s00454-004-1146-y

[77] Santoso, A., England, M.H., Kajtar, J.B., Cai, W.: Indonesian Throughflow Variability and Linkage to ENSO and IOD in an Ensemble of CMIP5 Models. J. Clim. **35**(10), 3161–3178 (2022). https://doi.org/10.1175/JCLI-D-21-0485.1

[78] Sun, S., Thompson, A.F.: Centennial Changes in the Indonesian Throughflow Connected to the Atlantic Meridional Overturning Circulation: The Ocean's Transient Conveyor Belt. Geophys. Res. Lett. **47**(21), 2020–090615 (2020). https://doi.org/10.1029/2020GL090615

[79] Peng, Q., Xie, S.-P., Huang, R.X., Wang, W., Zu, T., Wang, D.: Indonesian Throughflow Slowdown under Global Warming: Remote AMOC Effect versus Regional Surface Forcing. J. Clim. **36**(5), 1301–1318 (2023). https://doi.org/10.1175/JCLI-D-22-0331.1

[80] Xin, L., Hu, S., Wang, F., Xie, W., Hu, D., Dong, C.: Using a deep-learning approach to infer and forecast the Indonesian Throughflow transport from sea surface height. Front. Mar. Sci. **10** (2023). https://doi.org/10.3389/fmars.2023.1079286

[81] Susanto, R.D., Wei, Z., Santoso, P.D., Wang, G., Fadli, M., Li, S., Agustiadi, T., Xu, T., Priyono, B., Li, Y., Fang, G.: Field measurements of turbulent mixing south of the Lombok Strait, Indonesia. Geosci. Lett. **11**(36) (2023). https://doi.org/10.1186/s40562-024-00349-3

[82] Ray, R.D., Susanto, R.D.: Tidal mixing signatures in the Indonesian seas from high-resolution sea surface temperature data. Geophys. Res. Lett. **43**(15), 8115–8123 (2016). https://doi.org/10.1002/2016GL069485

[83] Li, A., Zhang, Y., Hong, M., Xu, T., Wang, J.: Asymmetric Response of the Indonesian Throughflow to Co-Occurring El Niño–Southern Oscillation–Indian Ocean Dipole Events. Remote Sens. **16**(18) (2024). https://doi.org/10.3390/rs16183395

[84] Fritz, M., Mayer, M., Haimberger, L., Winkelbauer, S.: Assessment of Indonesian Throughflow transports from ocean reanalyses with mooring-based observations. Ocean Sci. **19**(4), 1203–1223 (2023). https://doi.org/10.5194/os-19-1203-2023

[85] Furue, R., Nonaka, M., Sasaki, H.: The intrinsic variability of the Indonesian Throughflow. Front. Mar. Sci. **10** (2023). https://doi.org/10.3389/fmars.2023.1117304

[86] Xu, W., Yuan, D., Li, M.: Interannual Variability of the Indonesian Throughflow in the Makassar Strait Associated With the 2015/2016 Super El Niño. Geophys. Res. Lett. **52**(1), 2024–111709 (2025). https://doi.org/10.1029/2024GL111709